Synergized photothermal therapy and magnetic field induced hyperthermia via bismuthene for lung cancer combinatorial treatment

Açelya Yilmazer [a,b,*], Zafer Eroglu [c], Cansu Gurcan [a,b], Arianna Gazzi [e,l], Okan Ekim [f], Buse Sundu [c], Cemile Gokce [a], Ahmet Ceylan [g], Linda Giro [l], Mehmet Altay Unal [b], Fikret Arı [h], Ahmet Ekicibil [i], Ozge Ozgenç Çinar [g], Berfin Ilayda Ozturk [a], Omur Besbinar [a,b], Mine Ensoy [j], Demet Cansaran-Duman [j], Lucia Gemma Delogu [d,l,**], Onder Metin [c,k,***]

a Department of Biomedical Engineering, Faculty of Engineering, Ankara University, 06830 Ankara, Türkiye
b Stem Cell Institute, Ankara University, 06520, Ankara, Türkiye
c Department of Chemistry, Faculty of Science, Koç University, 34450, Istanbul, Türkiye
d Department of Biology, College of Arts and Sciences, Khalifa University, Abu Dhabi, UAE
e Department of Chemical and Pharmaceutical Sciences, University of Trieste, 34127, Trieste, Italy
f Department of Anatomy, Faculty of Veterinary Medicine, Ankara University, 06110, Ankara, Türkiye
g Department of Histology Embryology, Faculty of Veterinary Medicine, Ankara University, 06110, Ankara, Türkiye
h Department of Electrical Electronic Engineering, Faculty of Engineering, 06830, Ankara, Türkiye
i Department of Physics, Faculty of Arts and Sciences, Cukurova University, 01330, Adana, Türkiye
j Biotechnology Institute, Ankara University, 06135, Ankara, Türkiye
k Koç University Surface Science and Technology Center (KUYTAM), Istanbul, 34450, Türkiye
l Department of Biomedical Sciences, University of Padua, 35129, Padua, Italy

ARTICLE INFO

ABSTRACT

Thanks to its intrinsic properties, two-dimensional (2D) bismuth (bismuthene) can serve as a multimodal nanotherapeutic agent for lung cancer acting through multiple mechanisms, including photothermal therapy (PTT), magnetic field-induced hyperthermia (MH), immunogenic cell death (ICD), and ferroptosis. To investigate this possibility, we synthesized bismuthene from the exfoliation of 3D layered bismuth, prepared through a facile method that we developed involving surfactant-assisted chemical reduction, with a specific focus on improving its magnetic properties. The bismuthene nanosheets showed high *in vitro* and *in vivo* anti-cancer activity after simultaneous light and magnetic field exposure in lung adenocarcinoma cells. Only when light and magnetic field are applied together, we can achieve the highest anti-cancer activity compared to the single treatment groups. We have further shown that ICD-dependent mechanisms were involved during this combinatorial treatment strategy. Beyond ICD, bismuthene-based PTT and MH also resulted in an increase in ferroptosis mechanisms both *in vitro* and *in vivo,* in addition to apoptotic pathways. Finally, hemolysis in human whole blood and a wide variety of assays in human peripheral blood mononuclear cells indicated that the bismuthene nanosheets were biocompatible and did not alter immune function. These results showed that bismuthene has the potential to serve as a biocompatible platform that can arm multiple therapeutic approaches against lung cancer.

1. Introduction

According to Global Cancer Statistics 2020, lung cancer is the leading cause of cancer death worldwide [1]. The search for effective treatments for lung cancer remains an area of intensive research in the biomedical field. To this aim, scientists are exploring therapeutic approaches based on nanomaterial properties [2–4]. In recent years, extensive research has focused on exploring the ability of two-dimensional (2D) materials to be used in photothermal (PTT) or photodynamic therapy (PDT) for cancer [5–8]. Other studies have combined these materials with

immunotherapies to induce immunogenic cell death (ICD) after PDT/PTT induced apoptosis [9,10]. More recently, ferroptosis, a type of cell death, has received substantial interest, particularly in cancer cells resistant to apoptotic therapies. Therefore, ferroptosis therapy has been explored as an effective strategy in cancer nanotherapeutics [11–13]. However, combining these therapeutic approaches in a single nanoplatform has not previously been achieved.

2D materials have been proposed to be promising candidates for such applications, because of their extraordinary intrinsic properties including their specific surface area, adsorption capacity, visible-to-NIR light harvesting ability, and cytocompatibility [14–19]. The 2D materials of group 15 elements, namely 2D pnictogens (phosphorene, arsenene, antimonene, and bismuthene), have recently emerged as new members of the ever-growing 2D family that show outstanding electronic, topological, thermoelectric, and optical properties [20–22]. Among them, bismuthene (2D monolayer or few-layer bismuth) has notable properties such as low cost [23], low toxicity [24], and high stability under ambient conditions [25]. In addition, bismuthene shows unique electronic, magnetic, and optical properties compared to 3D layered bismuth owing to its size and number of stacking layers [26–28]. For example, 3D layered bismuth is considered a nonmagnetic semi-metal; in contrast, bismuthene exhibits semiconducting and slight magnetic properties due to the quantum confinement effect and its small bandgap, which can be tuned by the number of layers (0.3–1.0 eV) when the exfoliated layers are thinner than 30 nm (thinner than the Fermi wavelength) [29,30]. Metin and co-workers have reported the first example of the photocatalytic application of bismuthene in a liquid-phase chemical transformation proceeding on a radical pathway [31], suggesting its high promise in cancer therapy. Therefore, bismuthene has recently been proposed as a potential nanomaterial for photothermal cancer treatment, because of its outstanding photocatalytic activity in liquid-phase chemical reactions [32,33]. For example, Wang et al. have reported that bismuthene can be used as a photodynamic and/or PTT agent under near-infrared light irradiation [34]. Later, with its intrinsic optical absorbance and strong X-ray attenuation, a dual photonic therapy based on bismuthene nanoplatform can be conducted under the supervision of photoacoustic/computed tomography-guided multimodal imaging. Based on that, Bai et al. have synthesized a composite tetragonal bismuthene-based nanosystem, namely TPP-Bi@PDA@CP to be used in multimodal imaging and PTT at even lower doses. They have also concluded that this system has ability to inhibit the recurrence of tumor [35]. In another study, Zhu et al. have used modified form of bismuthene nanosheets (POBNS-PEG) for delivering the drug doxorubicin (DOX) effectively and founded that this material have both photothermal activity against tumors and photocatalytic activity by reducing CO_2 to CO in cancer cells, which could increase the drug sensitivity and decrease inflammatory response after tumor killing [36]. Additionally, in another study, Guo et al. have attempted to combine immunotherapy with PTT by coupling bismuthene with PD-L1 siRNA (Bi@PP/siRNA) [37]. The system releases siRNA after NIR irradiation, thus leading to a tumor-enhanced pathological permeability and retention effect, and an increase in TIL recruitment, thereby amplifying *anti*-PD-L1 immunotherapy [37]. However, this study have considered the aspect of the immune system from a therapeutic approach much rather than the immunocompatibility of the nanosystem. Generally, the immunocompatibility of other 2D nanomaterials like graphene based materials such as graphene oxide, graphitic carbon nitride, black phosphorous or MXenes such as niobium carbide (Nb_4C_3), vanadium carbide (V_4C_3) have been more extensively evaluated in previous studies compared to bismuthene [38–40]. The biocompatibility of bismuth-based nanosystems has been demonstrated *in vivo* and *in vitro*, but the key aspect of the effects of the nanomaterial on immune cells has not been elucidated [8,41].

Here, we demonstrate that bismuthene nanosheets are potential lung cancer nanotherapeutics that simultaneously enable PTT, MH, ICD, and ferroptosis. For this purpose, bismuthene nanosheets were prepared from the exfoliation of layered 3D bismuth (Bi) synthesized through a method that we developed involving surfactant-assisted chemical reduction, with a focus on improving its magnetic properties. The success of bismuthene-based cancer therapy was improved when the light and magnetic field exposure were combined synergistically, under both *in vitro* and *in vivo* experimental conditions. Based on these results, PTT activity of bismuthene predominates and shown to be further improved when combined with magnetic field. The results suggested that ICD and ferroptosis-dependent mechanisms were also involved during this augmented therapeutic effect. Furthermore, the material was found to be non-toxic and to show a high immune cytocompatibility profile, thereby suggesting its potential safety in future clinical applications.

2. Results

2.1. As-prepared bismuthene nanosheets show photothermal properties in cancer cells

First, to synthesize bismuthene nanosheets, 3D layered bismuth was synthesized by using a previously described surfactant-assisted chemical reduction method [31]. Next, bismuthene nanosheets were prepared through liquid phase exfoliation of the 3D layered Bi in DI water [31]. To reveal the crystalline structure and the surface chemical composition of the as-prepared bismuthene, we performed characterization with powder X-ray diffraction (*p*-XRD) and X-ray photoelectron spectroscopy (XPS) analysis. In the XRD pattern of as-synthesized bismuthene (Fig. 2A), three main peaks were observed at $2\theta = 27.2°$, $39.6°$, and $37.9°$, which were assigned to the (012), (110), and (104) diffraction planes of the rhombohedral crystal structure of Bi (β-Bi, PDF no: 04-006-7762) [37]. The deconvoluted XPS spectrum of the Bi 4f region (Fig. 2B) showed two sets of peaks at binding energies of 156.8/162.1 eV and 158.7/164.2 eV, which were attributed to the $4f_{5/2}$ and $4f_{7/2}$ core levels of metallic Bi and bismuth oxides, respectively. The peaks assigned to bismuth oxides were attributed to the partial oxidation of the bismuthene surface [31]. In order to get further insights into the resulting partial oxidation, a well-known method, XPS depth profile analysis was conducted by the Ar ion bombardment. The comparison of the XPS spectra before and after the Ar ion bombardment clearly revealed that the oxidation occurred mostly on the surface, not due to the formation of bismuth oxide compounds (Fig. S1F). To gain insights into the optical properties of the as-prepared bismuthene nanosheets, we recorded UV–vis–NIR diffuse reflectance absorption spectra between 300 and 1700 nm. On the basis of the DRS absorption spectrum depicted in Fig. S1A, we concluded that bismuthene has strong absorption bands in the NIR region with a layer-dependent bandgap property [42]. The Raman spectra of the as-prepared bismuthene and bulk Bi (Fig. S1B) showed two main peaks at 70.2 and 96.8 cm^{-1}, which were ascribed to the E_g and A_{1g} vibration modes of metallic Bi, respectively [43,44]. Notably, no peak was associated with bismuth oxides in the Raman spectra [44]. In comparison to the Raman spectra of bismuthene and 3D bismuth, the E_g and A_{1g} peaks of the bismuthene shifted to a higher wavenumber with lower intensity than those of bulk Bi, thus indicating that ultrasound-assisted liquid-phase exfoliation yielded few-layer bismuthene from the 3D layered Bi [45].

The topological, morphological, and compositional properties of the as-prepared bismuthene were analyzed by using scanning electron microscopy (SEM), atomic force microscopy (AFM), transmission electron microscopy (TEM), high resolution (HR) TEM, and high-angle annular darkfield scanning transmission electron microscopy (HAADF-STEM) associated EDS elemental mapping. The SEM image of bismuthene (Fig. 2C) verified its flake-like structure with a smooth surface and 600 nm lateral size. The AFM image and corresponding height profile of bismuthene in Fig. 2D confirmed that the bismuthene had a topographic height of 5.86 nm with a few layers 2D structure. A similar conclusion was reached on the basis of the TEM image of bismuthene (Fig. 2C), which revealed the formation of few-layer bismuthene from the
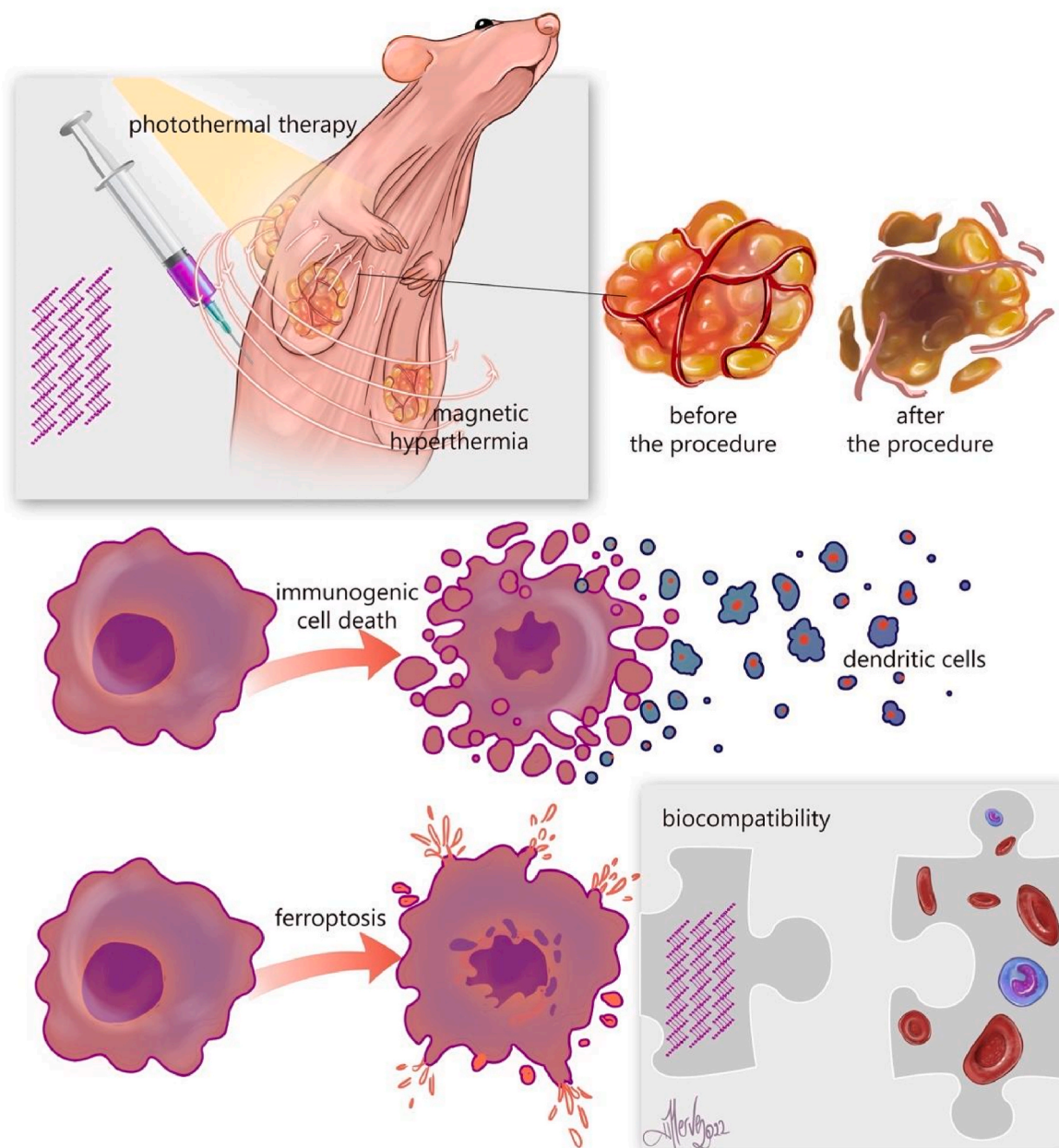
Fig. 1. Experiment workflow.

exfoliation of the bulk bismuth in DI water (Fig. 2E, Fig. S1E). According to the HR-TEM image in Fig. 2F, the lattice spacing of bismuthene was calculated to be 0.21 nm, which matched well with the (110) plane of rhombohedral bismuth [46,47]. The HAADF-STEM image and the associated EDS elemental mapping images of bismuthene (Figs. S1C and S1D) indicated its composition of uniformly distributed Bi atoms along with a trace amount of surface oxides. Beyond these detailed morphological and topological characterizations, the particle size distribution of bismuthene in DI water was analyzed with a zeta-sizer. As shown in Fig. 2G, the average particle size of exfoliated bismuthene nanosheets (hydrodynamic diameter) is 200 nm. Furthermore, a serum stability analysis was performed by analyzing the change in hydrodynamic diameter and zeta potential of bismuthene in 50% FBS in PBS. As it can be clearly seen from Fig. 2H, there was almost no change in the hydrodynamic diameter of bismuthene in the first 5 days, while a slight increase was observed after the 5th day. However, the hydrodynamic diameter remained stable thereafter (Fig. 2H). The increase in the

hydrodynamic diameter of bismuthene after the 5th day is probably due to protein adsorption on the bismuthene surface. These results indicate that the blood stability of bismuthene is suitable for *in vivo* applications.

2.2. Bismuthene nanosheets show magnetic properties that enhance anti-cancer activity

Alternating current (AC) susceptibility, and temperature-dependent and field-dependent magnetization measurements were conducted to investigate the magnetic properties of the as-prepared bismuthene nanosheets. Fig. 3A (i and ii) show *M-T* curves for ZFC (black) and FC (red) conditions between 5 and 350 K at 100 Oe and 250 Oe, and *M-H* curves 5, 37, 50, 300, 320, and 350 K. The ZFC/FC magnetization curves exhibited behavior characteristic of a weak ferromagnetic signal and irreversibility of the transition temperature close to room temperature for both applied fields of 100 and 250 Oe. The appearance of two maxima, which are scales with the field, in Fig. 4A (i) in the ZFC curves
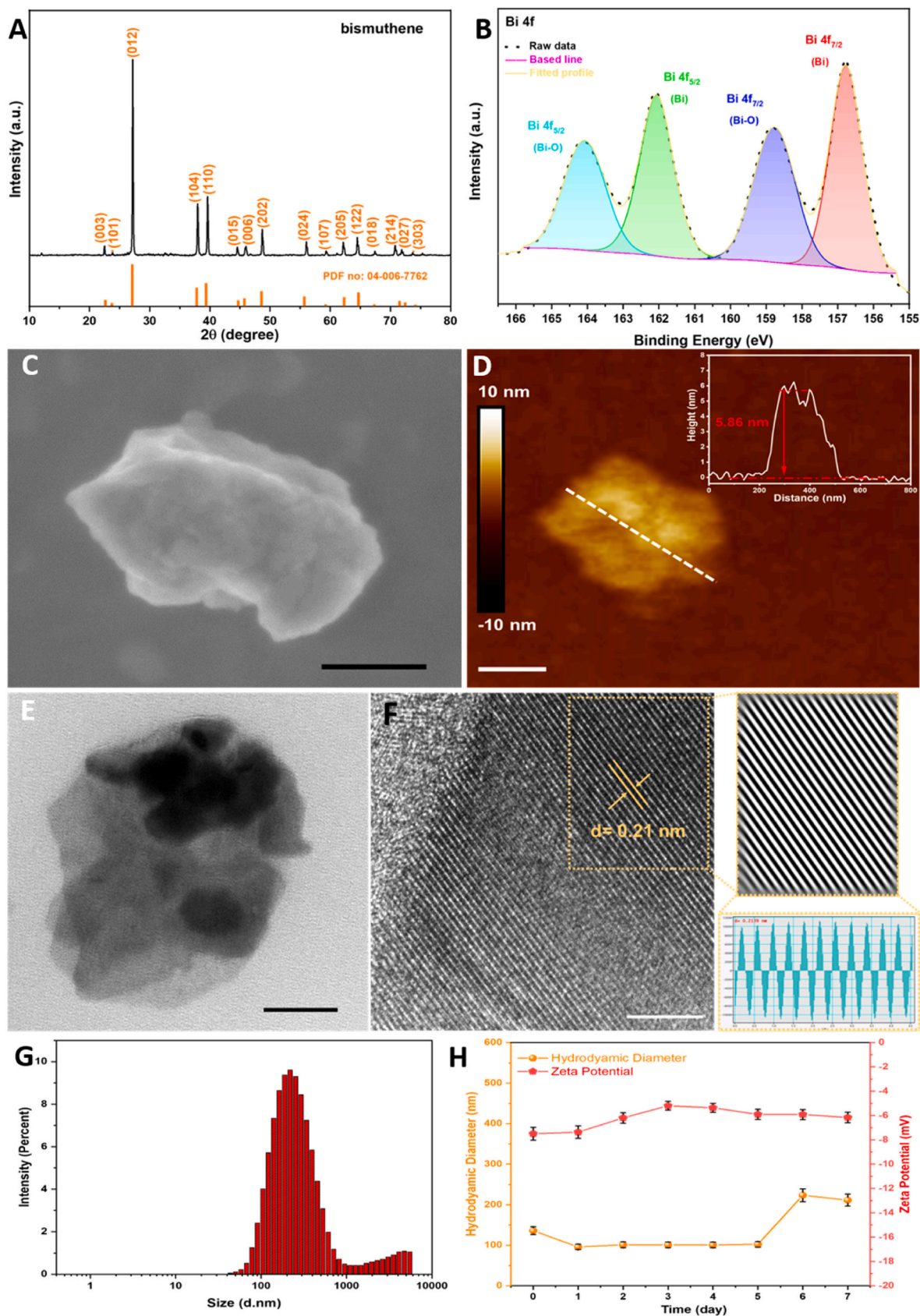
Fig. 2. Characterization of 2D bismuthene nanosheets. (a) XRD pattern, **(b)** High resolution XPS spectrum of core level of Bi 4f, **(c)** SEM image, the scale bar is 200 nm, **(d)** AFM image, and the corresponding height profile of bismuthene nanosheet, the scale bar is 100 nm, **(e)** TEM image, the scale bar is 200 nm, **(f)** HR-TEM image, IFFT of the selected region and Gatan digital micrograph-based lattice fringe calculation of bismuthene, the scale bar is 5 nm, **(g)** in aqueous suspension was analyzed by a zeta-sizer, **(h)** Hydrodynamic diameter evolution and Zeta potential measurements vs. time of bismuthene in PBS:FBS (1:1).
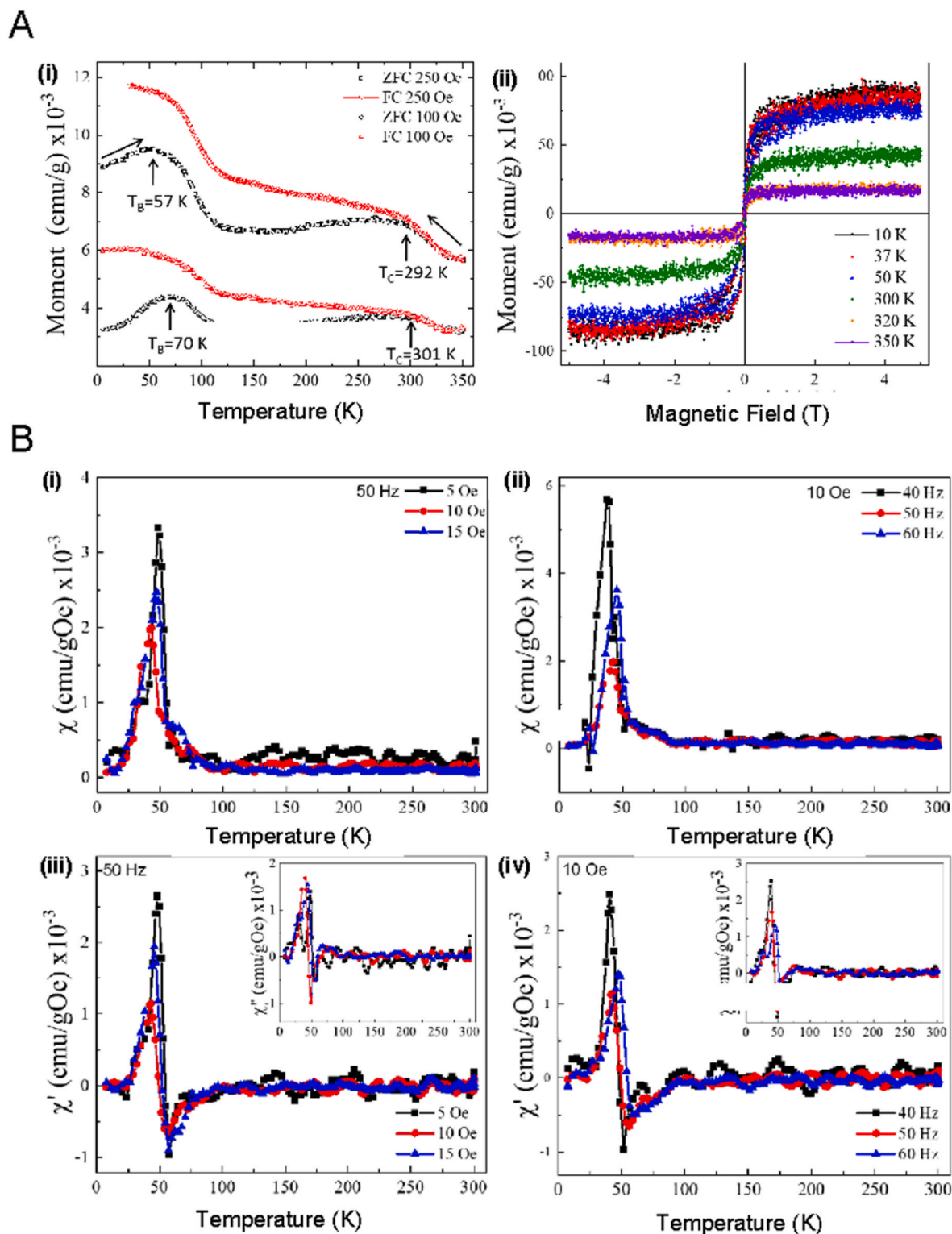
Fig. 3. Evaluation of 2D bismuthene mediated MH. (a) (i) ZFC and FC curves of M-T between 5 and 350 K with an applied field of 100 Oe and 250 Oe showing magnetic phase transition temperatures of TB and TC. (ii) M − H curves at 5, 37, 50, 300, 320, and 350 K up to the applied field of ±5 T. **(b)** (i and iii) χ, χ′, and χ″ curves for 5 (black), 10 (red), and 15 Oe (blue) at a constant frequency of 50 Hz. (ii and iv) χ, χ′, and χ″ curves for 40 (black), 50 (red), and 60 Hz (blue) at a constant magnetic field of 10 Oe.

at approximately 70 K corresponded to the blocking temperature (T_B). Therefore, the blocking of the magnetic moment of bismuthene with random orientation and 301 K was assigned to the critical temperature (T_C). Temperature-dependent hysteresis loops of bismuthene are presented in Fig. 3A (ii) at 5, 37, 50, 300, 320, and 350 K up to an applied

field of ±5 T after subtraction of the diamagnetic background. The coercive field (H_c) saturation magnetization (M_s), remanent magnetization (M_r), and remanence to saturation magnetization ratio (M_r/M_s) were determined from the M-H curves (Table 1). The maximum H_c was 498.5 Oe at 10 K and it disappeared at 350 K (77 °C). Bismuthene exhibited
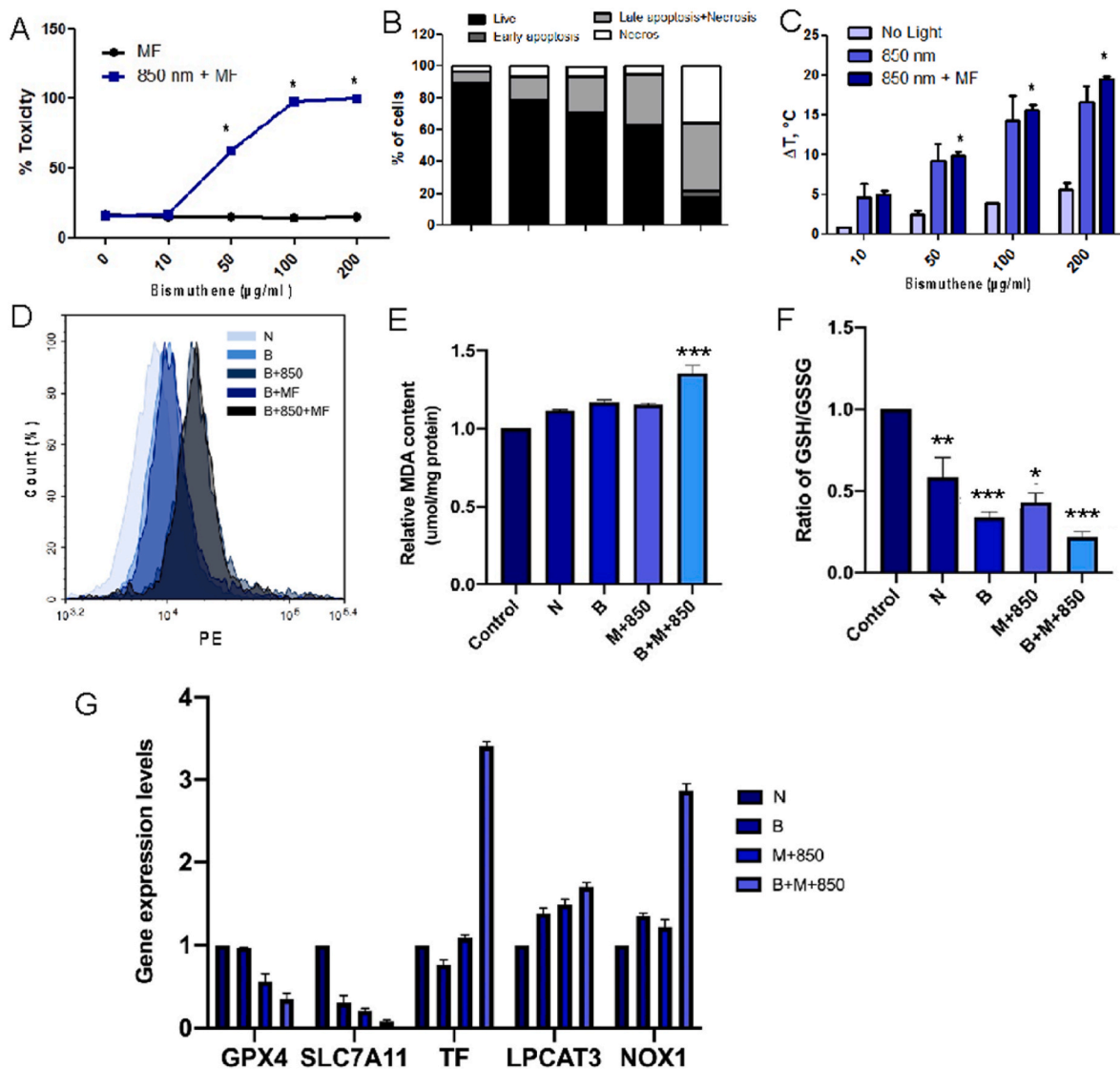
Fig. 4. *In vitro* evaluation of 2D bismuthene mediated by the combinatorial use of MH and PTT **(a)** A549 cells were treated with bismuthene at different concentrations (0, 10, 50, 100, 200 μg/mL) in complete media for 4 h at 37°C CO2 incubator followed by 1 h light (850 nm) irradiation and 50 Hz and 600 mA magnetic field exposure. Percentage of viability was assessed by modified LDH assay at 24 h (*p < 0.05 indicates statistically significant differences between the cell viability levels of magnetic field exposed and bismuthene + light + magnetic field exposed groups, obtained by the analysis of variance and Tukey's pairwise comparison). **(b)** Naïve (N), bismuthene treated (B), light irradiated (L), bismuthene treated and light irradiated (B + L) and bismuthene treated, light irradiated and magnetic field exposed (B + L + MF) cells were collected after 12 h and stained with PI and Annexin-FITC. Events (10,000) were counted and PI vs FITC plots were plotted in order to determine the populations of live, early apoptotic, late apoptotic/necrotic or necrotic cells. **(c)** Cells were treated with bismuthene (100 μg/mL) in complete media for 4 h at 37°C CO2 incubator followed by 1 h light (850 nm) irradiation and 50 Hz and 600 mA magnetic field exposure. At the end of exposure, temperature changed were recorded by thermal sensors inserted into the culture media. (*p < 0.05 indicates statistically significant differences between the temperature changes of naive and bismuthene + light + magnetic field exposed groups, obtained by the analysis of variance and Tukey's pairwise comparison). **(d)** Naïve (N), bismuthene treated (B), light irradiated (L), bismuthene treated and light irradiated (B + L) and bismuthene treated, light irradiated and magnetic field exposed (B + L + MF) cells were collected and stained with *anti*-calreticulin antibody. Cells were counted with a flow cytometer and percentage of positive cells were plotted. Cell culture supernatant was analyzed for the levels of **(e)** HMGB1 and **(f)** ATP. **(g)** MDA assay was performed to determine LPO levels. **(h)** GSH/GSSH ratios were determined by spectrophotometric analysis. **(i)** RNA was extracted from different treatment groups and the expression levels of key genes involved in ferroptosis were analyzed by qRT-PCR. Statistical differences: *p < 0.05, ***p < 0.001 compared to untreated control group or indicated group by one-way ANOVA followed by a Tukey's post hoc multiple comparisons.

properties of a soft magnetic material with a moderate coercivity of 128.5 Oe at 320 K (47 °C), allowing the heat generated during treatment to be controlled [48]. Similarly, M_s and M_r decreased with an increase in temperature to 350 K. The hysteresis loops began to show saturation beyond 0.4 T, which is less than the standard magnetic field strength used in magnetic resonance imaging. The recorded M_r/M_s ratio was less than 0.24, thus indicating that the soft magnetic behavior was due to the internal stress that resulted in the uniaxial magnetic anisotropy in the bismuthene structure. We also calculated the effective magnetic

moment (μ_{eff}) of bismuthene according to the equation, $\mu_{eff}=(M\,M_s)/(N_A\,\beta)$. Here, β is the conversion factor (9.27×10^{-21} Erg/Oe), M is the molecular weight (212 g/mol), M_s is the saturation magnetization obtained from the *M-H* curve, and N_A is Avogadro's number. The maximum μ_{eff} value was $3.3 \times 10^{-3}\mu_B$ for 10 K, and it decreased with increasing temperature (Table 1). Moreover, we also calculated specific loss power (SLP) using the M − H curves at 300 K and 320 K (close to body temperature) and used parameters and calculated SPL values were reported in Table S1. The SLP value decreased from 3193.2 W/g to 1576.5 W/g

Table 1

Analysis of *M-H* curves for coercive field (H_c), saturation magnetization (M_s), remanent magnetization (M_r), remanence to saturation magnetization ratio M_r/M_s, and effective magnetic moment μ_{eff} at 5, 37, 50, 300, 320, and 350 K.

Temperature (K)	H_c (Oe)	M_s (emu/g) $\times 10^{-3}$	M_r (emu/g) $\times 10^{-3}$	M_r/M_s	μ_{eff} (μ_B) $\times 10^{-3}$
10	498.5	87	21	0.24	3.3
37	459.0	84	18	0.21	3.2
50	328.5	75	16	0.21	2.8
300	196.5	44	3	0.07	1.7
320	128.5	19	2	0.11	0.7
350	–	17	1	0.06	0.6

with increasing temperature from 300 K to 320 K. These results indicate that tumor treatment is possible with bismuthene treatment.

The coil magnetization value with an applied current of 0.6 A and frequency of 50 Hz on the tumor cell region was estimated to be 10 Oe. Accordingly, the AC susceptibility χ, χ′, and χ″ values were determined for 5 (black), 10 (red), and 15 Oe (blue) at a constant frequency of 50 Hz and χ, χ′, and χ″ curves for 40 (black), 50 (red), and 60 Hz (blue) at a constant magnetic field of 10 Oe (Fig. 3B (i-iv)). We observed negligible susceptibility at 300 K, similar to χ′, and χ″; decreasing the temperature below 100 K resulted in an increase around 50 K because of noninteracting or weakly interacting 2D bismuthene structures. Furthermore, χ′ and χ″ exhibited clear negative values, which were attributed to the diamagnetic property of Bi. The further increase was due to the ferromagnetic signal in the bismuthene structure. Frequency-dependent measurements also revealed similar phase transitions, but decreasing the frequency to 40 Hz increased the χ value and resulted in a shift to a lower temperature. Therefore, very weak AC susceptibility around 300 K was observed under applied fields of 5, 10, and 15 Oe for 50 Hz constant frequency. The magnetic results revealed that all samples had a weak ferromagnetic characteristic that appeared only after diamagnetic background subtraction. It is found that the phase transition on *M-T* and AC susceptibility curves was due to blocking magnetic spins and the diamagnetic contribution from Bi atoms in the structure. Small H_c and M_s were found to be 489.5 Oe and 87×10^{-3} emu/g, respectively.

2.3. Bismuthene nanosheets can synergistically combine MH with PTT in vitro and activate immunogenic cell death and ferroptosis

The photothermal activity of bismuthene nanosheets was evaluated in the A549 lung adenocarcinoma cell line. First, A549 cells were treated with the bismuthene nanosheets (100 µg/mL) and exposed to light at 850 nm for 1 h. Compared with the no-light group, the bismuthene treated and light-exposed groups showed concentration-dependent cell death (Fig. S2A). In cells treated with bismuthene at 100 µg/ml dose and exposed to 520 nm light, there is no effective cancer cell killing activity, the number of cells increased compared to untreated naïve groups. However, there is no statistical significance observed for this group compared to the naive and therefore can be counted negligible. As expected, the exposure time was also found to be a critical parameter influencing cell death. As shown in Fig. S2B, increasing the light exposure time augmented the bismuthene-dependent toxicity in A549 cells. When light sources at different wavelengths were used, bismuthene showed the highest toxicity at 850 nm light irradiation. The light at other wavelengths (590 nm and 625 nm) also resulted in up to 30% and 40% cell death, respectively (Fig. S2C). These data suggested that bismuthene showed both PDT and PTT activity depending on the wavelength of light. To further demonstrate this conclusion, we performed DCFDA staining on bismuthene treated and light-exposed cells (Fig. S4). Confirming the viability result, the ROS generation was more prominent at 520, 625 and 940 nm light. According to our earlier study, bismuthene has a relatively narrow bandgap (0.69 eV) which can only produce •OH radicals [31,49] through in situ formed hydrogen peroxide decomposition based on its conduction band and its related

thermodynamical oxidation potential ability [31]. Therefore, we mainly focused its photothermal and magnetic field properties in order to achieve an effective anti-cancer activity.

Bismuthene-treated A549 cells were simultaneously exposed to 850 nm light and a magnetic field (50 Hz, 600 mA). As shown in Fig. 4A, simultaneous light and magnetic field exposure resulted in 100% cell death in A549 cells. These findings were further supported by apoptosis assays in which cells were stained with Annexin-FITC/PI after various treatments. Both necrosis and apoptosis were found to play roles in cell death after simultaneous light and magnetic field exposure to bismuthene-treated cells (Fig. 4B). To demonstrate that magnetic field exposure resulted in hyperthermia, we analyzed temperature changes in culture media. As shown in Fig. 4C, the highest temperature change was obtained when the cells were exposed to both light irradiation and a magnetic field, and the effect was concentration-dependent. PDT- and PTT-dependent tumor cell death is well known to result in ICD, activating immune cells. The surface expression of calreticulin is an important indicator of ICD [9]. Therefore, to show that simultaneous light and magnetic field exposure of bismuthene induced ICD, we stained treated cells with *anti*-calreticulin antibody and analyzed them through flow cytometry. As shown in Fig. 4D, the expression of calreticulin was significantly higher in the dual exposed and bismuthene treated A549 cells, thus indicating that bismuthene-based PTT and MH induced ICD. In addition to calreticulin expression, levels of ATP or HMGB1 in cell culture media are other markers of ICD. As can be seen in Fig. 4E and F, both HMGB1 release and extracellular ATP levels were significantly higher in bismuthene treated cells following both 850 nm light irradiation and magnetic field application.

Finally, to explore the involvement of ferroptosis during this combinatorial treatment, we performed MDA and GSH/GGSG assays. MDA assays determine the level of lipid peroxidation (LPO) within cells—a major feature of ferroptosis [13]. GSH depletion also promotes LPO through deactivating glutathione peroxidase 4 (GPX4), a key player in ferroptosis [13]. As shown in Fig. 4E, bismuthene treated and dual exposed A549 cells showed significantly higher MDA levels than cells in the other treatment groups, and additionally showed the greatest GSH depletion among experimental groups (Fig. 4F). To further delineate the underlying mechanism, we performed qRT-PCR of key genes (*GPX4* and *SLC7A11*, *TF*, *LPCAT3*, and *NOX1*) involved in ferroptosis. Chen et al. have emphasized that inhibition of *SLC7A11* causes GSH depletion and the subsequent inactivation of *GPX4*, thereby causing ferroptosis. In contrast, increased expression of *TF*, *LPCAT3*, and *NOX1* genes is also crucial for LPO and the induction of ferroptosis [50]. *GPX4* and *SLC7A11* were significantly more downregulated in the bismuthene treated and dual exposed cells than the other treatment groups (Fig. 4G). The expression of *TF*, *LPCAT3*, and *NOX1*, in contrast, was upregulated in the bismuthene and dual exposed groups (Fig. 4G). Together, these data suggested that ferroptotic mechanisms are involved in bismuthene-based PTT and MH.

In addition, we performed TEM analysis on thin sections of bismuthene-treated cells. The TEM images (Fig. S3) revealed that material was effectively taken up via phagocytosis/endocytosis by A549 cells, as evidenced by the presence of bismuthene nanosheets within vesicles in the cytoplasm. This result is also in line with other studies in literature reporting that bismuthene nanosheets can be internalized via endocytic pathway [34,36,37]. As shown in Fig. S4, even bismuthene exposure at 10 µg/mL resulted in a bright green signal in the cytoplasm, thus indicating that reactive oxygen species formed during the PDT protocol. After bismuthene-treated cells were exposed to 850 nm light, significant temperature changes were observed in the cell culture media (Fig. S2D).

2.4. Bismuthene nanosheets can synergistically combine MH with PTT in vivo and activate immunogenic cell death and ferroptosis

To further confirm the effectiveness of the photoactive and MH

properties of bismuthene, we performed an *in vivo* study. First, we injected tumor-bearing nude mice with 1000 μg of bismuthene nanosheets via the tail vein. At the 24 h time point, we performed ICP-MS analysis of all organs to evaluate the biodistribution of the material. Bismuthene showed uptake in the spleen and liver, with a lower percentage in the lung and bladder (Fig. 5B). Bladder accumulation might also suggest urine excretion, as has been observed for other 2D materials [8]. An *in vivo* setup was prepared for a dual PTT and MH protocol (Fig. 5C). A549 tumor xenografts were generated in Nude BalbC mice, and the treatment protocol was started when tumors reached approximately 200 mm³. After intravenous injection of the material, mice were anesthetized and exposed to 850 nm light irradiation and magnetic field simultaneously for 1 h. This treatment regime was repeated four times until day 19 (Fig. 5A). As shown in Fig. 5D, no significant change in body weight was observed during the entire duration of the study in any experimental group. Fig. S6 showed that at the end of 850 nm light irradiation and magnetic field exposure, the local tumor temperature was increased up to 47C in bismuthene-injected animals. This significant temperature increase indicated that we can successfully induce PTT and magnetic field-induced hyperthermia at the tumors. Tumor measurements showed that dual exposure to light irradiation and a magnetic field resulted in significant tumor growth inhibition in mice injected with bismuthene compared with mice in other treatment groups (Fig. 5E). Confirming these data, histological analysis of the tumors further suggested that tumors in bismuthine-injected mice exposed to both light irradiation and a magnetic field showed distinct anti-tumor activity. Apoptosis and progressive secondary necrosis, as evidenced by the presence of shrunken cells showing nuclear changes, were observed in these sections (Fig. 5F). Later, organs were paraffin-embedded and sectioned for Mallory's trichrome staining to evaluate the possible toxicity at the tissue level. Light microscopy showed no significant toxicity in any organ (Fig. S5).

We also immunostained tumor sections with anti-CD11c and anti-CD56 antibodies, to correlate with the calreticulin analysis *in vitro*. The expression of ICD markers, such as calreticulin, resulted in the recruitment of both dendritic cells (DCs) and cytotoxic cells, such as T cells or natural killer cells. Because the *in vivo* experiments were performed in Balb/C nude mice, we reasoned that natural killer cells might have been the cytotoxic cells that contributed to the anti-tumor activity. Therefore, we stained the tumor sections with anti-CD11c and anti-CD56 antibodies to track DCs and NK cells, respectively. As shown in Fig. 5G and H, tumor sections obtained from the B and B+850 nm + MF groups showed dense staining with anti-CD11c and anti-CD56 antibodies, respectively. The positive signals in these groups were distributed throughout the tumor sections, whereas the naïve and 850 nm + MF groups showed localized positive staining for these markers. These results suggested that efficient bismuthene accumulation, distribution, and diffusion were achieved throughout the tumors, thus augmenting the immune response through ICD, in addition to the PTT- and magnetic field-induced hyperthermia.

Finally, in parallel with the *in vitro* ferroptosis analysis, we further stained tumor sections to assess the involvement of ROS. A nonferrous ferroptosis therapy has been found to achieve maximal cell death through the integration of a synergetic ROS burst and GSH depletion into one nanoplatform [13]. Similarly, when we stained the tumor sections with a DCFDA kit, we observed positively stained regions in only the B+850 nm + MF group (Fig. 5I), thus suggesting that LPO and ferroptotic mechanisms were active in this combinatorial treatment strategy.

2.5. Bismuthene nanosheets are highly biocompatible

The cytocompatibility of bismuthene was initially assessed in whole blood, through observation of the hemolysis levels induced by increasing concentrations of bismuthene (10, 50, 100, 200 μg/mL) suspended in water, on red blood cells (RBCs). Changes in human whole blood were observed after 1 and 24 h treatment. No significant release of hemoglobin, which is correlated with RBC damage, was observed after bismuthene incubation (Fig. 6A). On the basis of our previous experience with graphene and other 2D-nanomaterials [47], we chose a sub-cytotoxic concentration of 100 μg/mL and a time-point of 24 h to ensure noticeable changes in immune cell activity (Fig. 6A). Complete blood counts were determined. We assessed changes in the numbers of RBCs, platelets, and total white blood cells subdivided into neutrophils, lymphocytes, and monocytes. Changes in the hematocrit, amount of hemoglobin, mean corpuscular volume, mean corpuscular hemoglobin (MCH) and its concentration (MCHC), red blood cell distribution width, and hemoglobin distribution width were also analyzed. Comparison of values of bismuthene-treated samples were compared with those of the corresponding untreated controls suggesting the high hemocompatibility of bismuthene (Fig. 6B). We also performed a cytocompatibility assessment in L929 healthy fibroblasts in which a dose dependent cytotoxicity was obtained until the 100 μg/mL concentration (Fig. S8).

Through the flow cytometry, we assessed viability and cell functionality in human peripheral blood mononuclear cells (PBMCs). The effects of bismuthene on cell viability were studied through live/dead staining with Fixable viability staining 780 (BD). PBMCs were incubated for 24 h with bismuthene (100 μg/mL) suspended in water, and the positive control was incubated with 70% ethanol. The higher percentage of living cells in the bismuthene-treated sample than the positive control (Fig. 7A) indicated that bismuthene treatment had no effect on immune cell viability. The expression of two important activation markers, CD25 (α-chain of the IL-2 receptor) and CD69 (C-Type lectin protein), was used to assess the functionality of T cells and monocytes, two representative populations of PBMCs. Monocytes and PBMCs showed non-significant changes in marker expression; however, T cells showed a significant decrease in the percentage of CD25⁺ and HLA-DR + populations (Fig. 7B). We also used flow cytometry assays to examine the potential activation of PBMCs after material treatment by testing the release of a wide range of cytokines, including IL-4, IL-5, IL-6, IL-10, IL12p70, TNFα, and IFNγ. Bismuthene (100 μg/mL) did not significantly affect the expression of the cytokines, thus further establishing its immunocompatibility (Fig. 7C).

3. Discussion

Post-carbon 2D materials, such as pnictogens, transition metal dichalcogenides, and boron nitride, have attracted substantial attention because of their intrinsic characteristics and photoactive properties [33]. These materials may provide a promising alternative for the next generation of biomedical tools by offering novel opportunities that cannot be achieved via carbon-based nanomaterials [51]. Especially in complex diseases such as lung cancer, for which traditional therapies fail to address efficacy and safety issues, 2D materials with novel physiochemical properties may provide an invaluable tool.

In the current study, we successfully demonstrated that dual exposure to 850 nm irradiation and a 50 Hz magnetic field resulted in high levels of cell death in bismuthene-treated A549 cells. By synthesizing 3D layered bismuth via a SACR method, we successfully generated bismuthene nanosheets in a controlled manner. These bismuthene nanosheets showed successful complementation of photo-activity with magnetic properties, thus enabling PTT and MR simultaneously. No other 2D material has been described in the literature to have both these properties simultaneously and most 2D materials have even no magnetic properties [52]. On the other hand, existing magnetic properties of bismuthene can be also enhanced slightly by doping it with non-metal atoms like carbon, silicion and germanium [53]. When it comes to iron-based nanomaterials, such as iron oxide nanoparticles (IONPs), they have unique magnetic properties and thus can be used in cancer therapy or diagnosis [54,55]. They exhibit MH induction or enhancement of immunotherapy when exposed to a high-frequency alternating magnetic field (AMF) [56–58]. These superparamagnetic IONPs
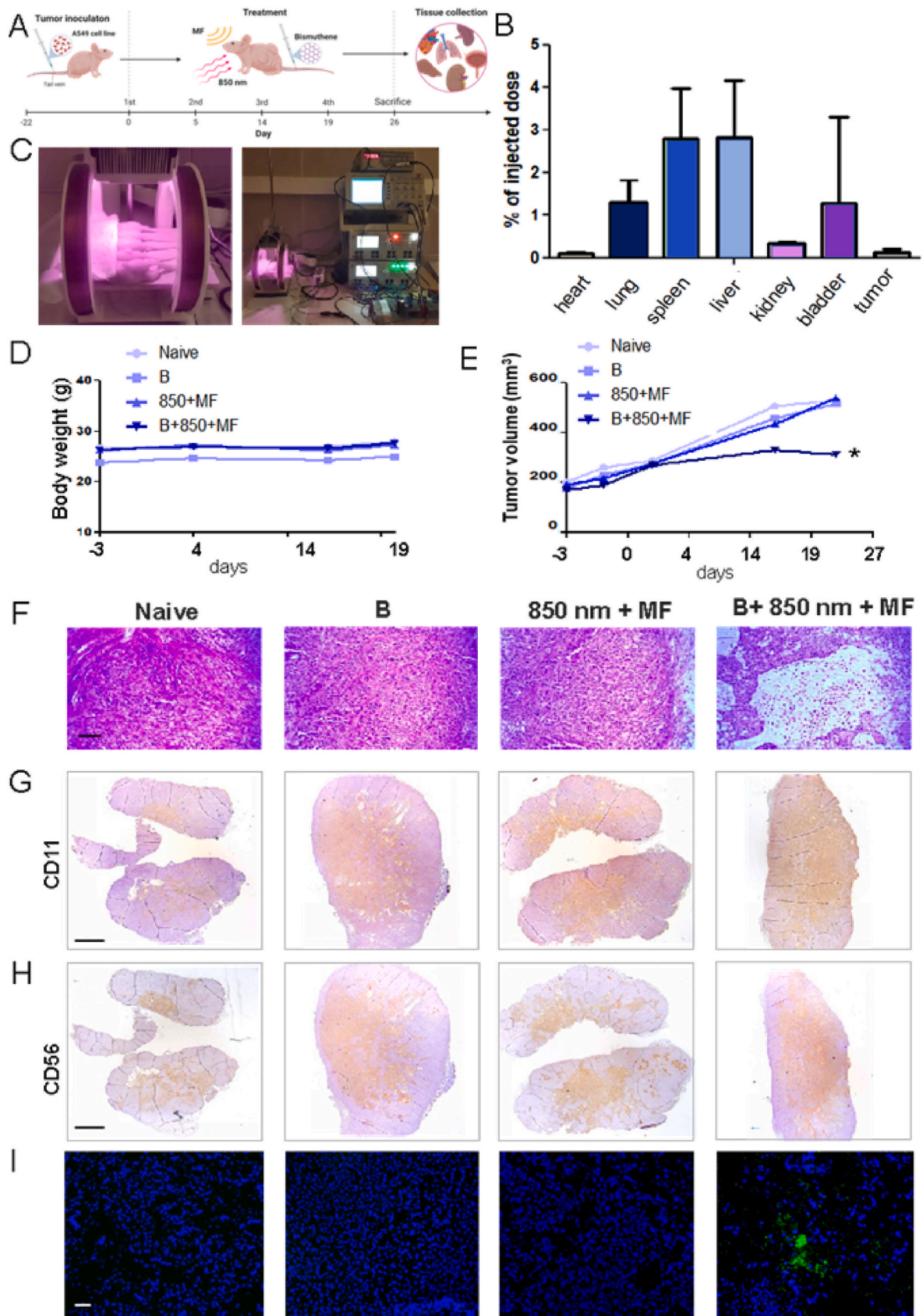
(caption on next page)

Fig. 5. *In vivo evaluation of bismuthene mediated anti-tumor activity.* **(a)** Following tumor cell inoculation, treatment protocol started at day 22 when the tumors reached around 200 mm^3. One hour after bismuthene administration, mice were anesthetized and exposed to 850 nm light and 50 Hz magnetic field. This procedure was repeated for 4 times and at the end of 27 days, mice were euthanized. **(b)** Nude mice bearing A549 xenografts were injected with 1000 µg bismuthene nanosheets intravenously. After 24 h, organs and tumors were collected and analyzed by ICP-MS in order to plot percentage of injected dose per each organ (*p < 0.05 indicates statistically significance between naive and bismuthene injected mice, obtained by the analysis of variance and Tukey's pairwise comparison). **(c)** Mice were subjected to light irradiation and magnetic field under anesthesia. Magnetic field was generated with an in-house constructed coil which was also combined with the LED light source. Representative images were obtained during the procedure. **(d)** Mice were monitored for body weight changes throughout the experimental duration. **(e)** Tumor volume growth was plotted against time for different experimental groups. (*p < 0.05 indicates statistically significant differences between the naive and treatment groups, obtained by the analysis of variance and Tukey's pairwise comparison). **(f)** Tumors were dissected and stained with Mallory's trichrome stain. Representative images were obtained with a light microscope. Scale bars represent 100 µm. In order to determine the presence of DCs and NKs at the tumors, sections were immunostained with **(g)** anti-CD11c and **(h)** anti-CD56 antibodies, respectively. Images were obtained with a light microscope to show the whole section for each group. Scale bars represent 500 µm. **(i)** DCFDA staining, scale bars represent 50 µm *p < 0.05, ***p < 0.001 compared to untreated control group or indicated group by one-way ANOVA followed by a Tukey's post hoc multiple comparisons.

generally suffer from low sensitivity to tumor diagnosis. Iron carbide nanoparticles (ICNPs) have higher stability, improved MRI contrast ability than iron oxide nanoparticles, which is good in clinical prospect but still it is early due to the problems of preparing pure iron carbide nanoparticles, non-uniformity during carbonization process leading to high toxicity, and lack of knowledge about their surface modification [54]. Soft ferromagnetic properties and moderate coercivity, preventing the hysteresis loss are much more desirable in MH-related tumor therapy [54,59]. For instance, Fe_5C_2 and Fe_2C nanoparticles, have been demonstrated to be soft magnetic NPs with a reduced coercivity, about 200 and 420 Oe respectively, which are safe considering the limit of applied magnetic fields [54,59]. Fe_5C_2 nanoparticles have also known to possess magneto-photo-thermal therapeutic features, which could be useful for hyperthermia-based cancer therapy [60]. Other than iron containing nanoparticles, other 2D materials have been suggested to achieve simultaneous PTT and MH for cancer therapy. For example, Cheng et al. have shown that Bi_2Se_3 with magnetic $FeSe_2$ nanoparticles can be used for combinatorial photothermal and radiation therapies, as confirmed by the high NIR absorption and strong X-ray attenuation of this hybrid nanostructure [61]. Other studies have combined iron oxide with various nanoparticles, including gold, silver, or silica, to boost hyperthermia with PTT [62–64]. However, achieving both activities in a single material would be desirable to achieve faster and more reproducible material batches. This aspect is highly important for the development of cancer nanotherapeutics [65,66]. Delivering anti-inflammatory drugs is an important strategy in the field of nanomedicine [67]. As the link between cancer and inflammation is further explored, nanoscientists may engineer novel nanomaterials to simultaneously combat tumor-associated inflammation and cancer carcinogenesis, dissemination, and metastasis.

An AC magnetic field results in heat dissipation via an applied frequency and a low-magnitude magnetic field [68]. In determining the heat dissipation, the AC susceptibility, χ, is a key value affecting the intrinsic properties of materials [69]. χ comprises the real part, χ', which indicates the slope of the *M-H* curve, and the imaginary part, χ'', which indicates the presence of dissipative processes in the sample [70,71]. Moreover, an AC magnetic field itself can cause tissue damage due to excessive heat, which can be controlled by the applied frequency, and also induces current. Specifically, tissue heating is negligible at very low (~0–300 Hz) and low (~300–100 kHz) frequencies [72], and the typical applied magnetic field used in hyperthermia is approximately 100–300 Oe [73]. Therefore, the applied magnetic field during this study did not cause any damage to healthy tissue, as confirmed by our *in vivo* results. Temperature-dependent magnetization, *M-T*, provides intrinsic magnetic properties of materials such as blocking (T_B), critical (T_c), Curie (T_C), and Neel (T_N) temperatures [74,75]. *M-T* curves revealed two magnetic phase transitions around 300 K (27 °C) and below 70 K, which were attributed to irreversible magnetic behavior and blocking of magnetic spins, respectively. Small hysteresis was observed after the subtraction of the diamagnetic background, and the maximum H_c and M_s were 489.5 Oe and 87×10^{-3} emu/g, respectively. Bismuthene exhibits soft magnetic material properties with a moderate coercivity of

128.5 Oe at 320 K (47 °C), thereby allowing the heat generated during the treatment to be controlled. Together with the *in vivo* results, the observed coercivity values and very weak AC susceptibility of bismuthene indicated that moderate heat generation occurred as a function of treatment time at the tumor location.

We also demonstrated that both ICD and ferroptosis mechanisms are involved in the bismuthene-based combinatorial therapeutic approach, thus directly explaining the augmented anti-cancer activity in lung adenocarcinoma cells. *In vitro* results suggested that exposure of bismuthene nanosheets to dual light plus a magnetic field augmented ICD activity, as evidenced by the increased expression of calreticulin and levels of extracellular ATP and HMGB1. Furthermore, tumor tissues in this experimental group showed high levels of DC and NK cell accumulation throughout the tumors, thus further suggesting that ICD-dependent immunotherapy works synergistically with PTT and MH *in vivo*. Beyond ICD analysis, we performed several assays to evaluate ferroptosis levels after bismuthene based PTT and MH both *in vitro* and *in vivo*. Recent studies have suggested that nanoparticles can be used to combine PTT and ferroptosis therapy and consequently achieve enhanced therapeutic activity [11,12]. Such an improved anti-cancer activity may rely on the fact that intracellular ROS and membrane LPO during the ferroptosis inhibit the expression of heat shock proteins which are the self-protection mechanism of cancer cells in response to heat during PTT [76,77]. Another mechanism could be through the PTT induced depletion of glutathione (GSH), thereby inducing PTT-enhanced ferroptosis via the reinforced inactivation of GPX4 [11]. Finally, it has been reported that when the environmental temperature increases from 20 to 50 °C, a significant increase can be observed in the rate of Fenton reaction which is important for the intracellular LPO accumulation [78]. Therefore, our study provides an important contribution to the field by demonstrating that bismuthene, owing to its intrinsic properties, can successfully kill cancer cells through multiple anti-cancer mechanisms.

To the best of our knowledge, this is the first report suggesting that biocompatible bismuthene-based PTT and MR can show effective anti-cancer activity simultaneously with ICD and ferroptosis dependent mechanisms. Further exploration of this novel multimodal material in therapeutic or even theranostic applications for other types of cancer will be crucial. Recently, other groups have started to investigate the possibility of developing double targeted bismuthene nanoplatforms [35], however selecting the best targeting group on cancer cells and adding functional antibodies or corresponding ligands on the surface of the nanomaterial are still limitation of the targeted nanoparticles [79–81]. Therefore, future studies can also consider the possibility of including a novel targeting moiety on our materials in order to improve its tumor accumulation.
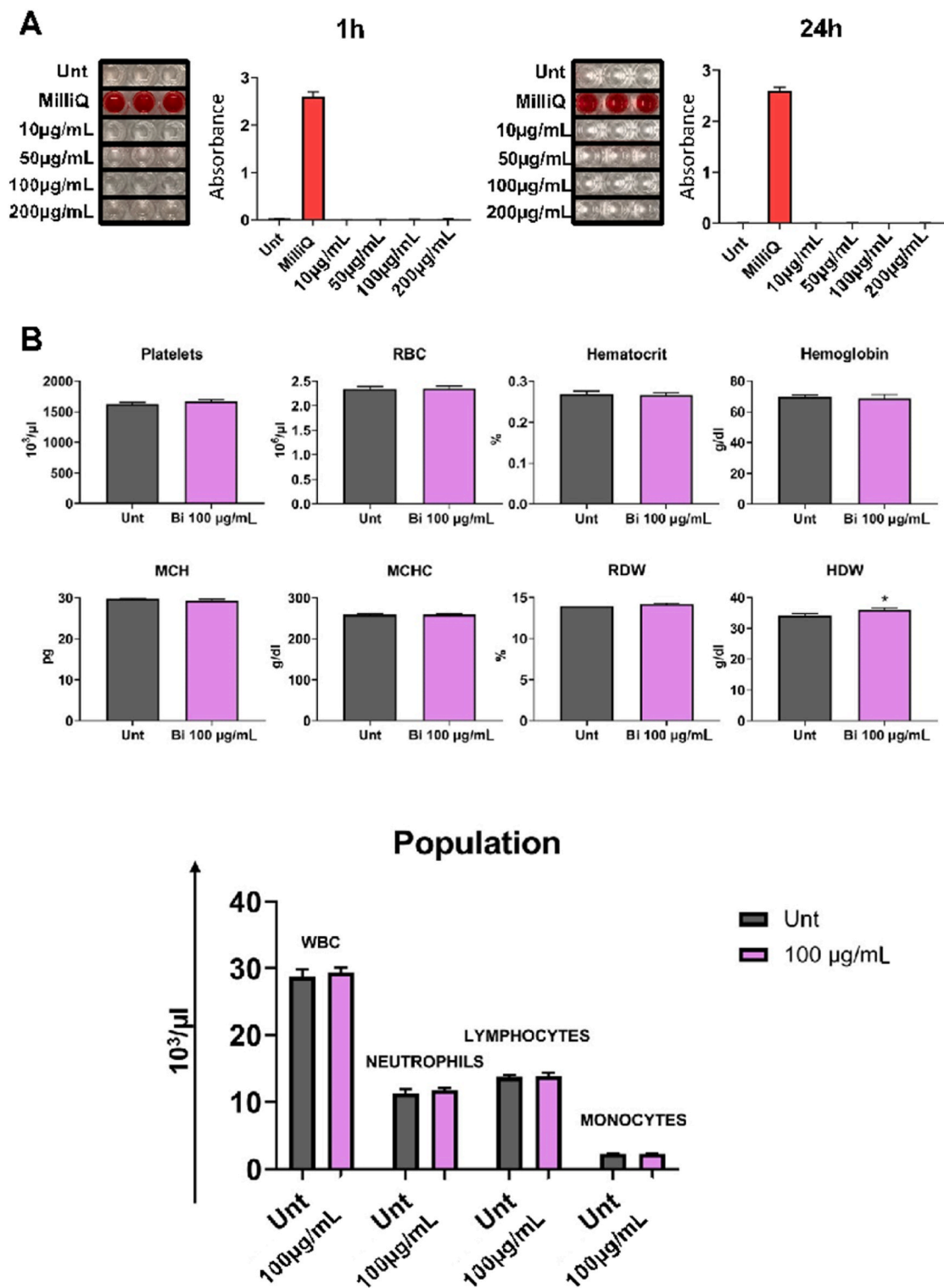
Fig. 6. *Ex-vivo* **bismuthene immunocompatibility in whole blood (a)** Hemolysis. Bismuthene (10, 50, 100 or 200ug/mL) was incubated with red blood cells (RBCs) for 1 and 24h. Pictures of human RBCs treated with the nanomaterial. The red color of the solution is due to the release of hemoglobin from the lysed RBCs. Positive control (RED) was treated with MilliQ water to induce cell lysis. Sample Absorbance was measured with Sunrise TECAN Infinite M200PRO microplate reader at the wavelength of 570 nm–620nm. Experiments were performed in triplicate. **(b)** Changes in human whole blood after the treatment with bismuthene 100ug/mL for 24h. Whole blood was harvested from healthy donor and incubated with 100 μg/mL bismuthene or left untreated (Unt). After 24h complete blood counts were performed. Changes in the number of red blood cells (RBC), platelets (PLT), total white blood cells (WBC), then divided into neutrophils (NEUTR), lymphocytes (LYMPH) and monocytes (MONO), were analyzed. Changes in hematocrit (HCT), amount of hemoglobin (HGB), mean corpuscular volume (MCV), mean corpuscular hemoglobin (MCH) and its concentration (MCHC), red blood cell distribution width (RDW) and hemoglobin distribution width (HDW) were also monitored. Data are presented as mean + - SD. Values of bismuthene-treated samples were compared to the corresponding untreated control using Welch's *t*-test and 2-way ANOVA.
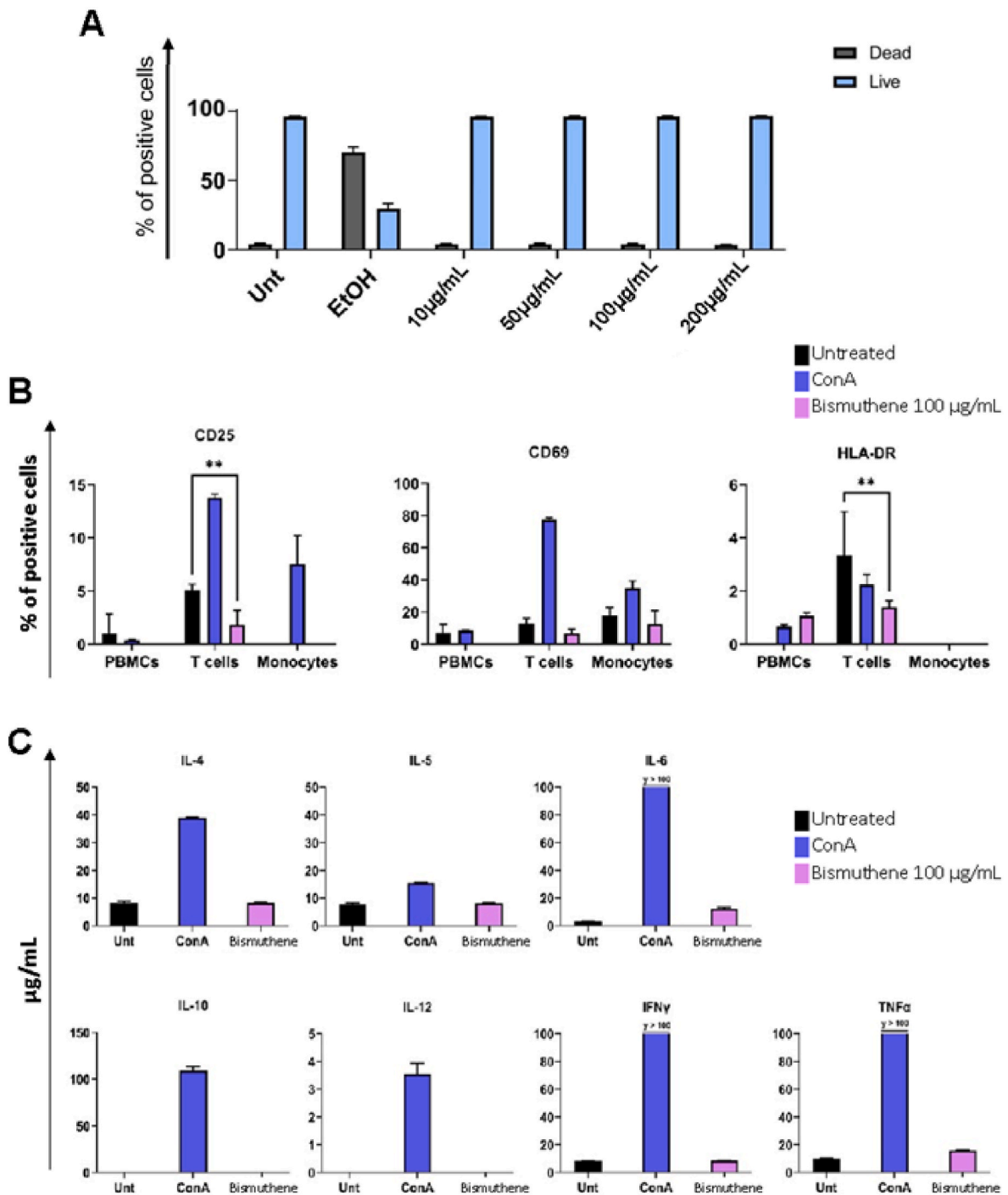
Fig. 7. *Ex-vivo* **bismuthene immunocompatibility in PBMCs (a)** Impact of bismuthene on PBMC viability. PBMCs were treated with different concentrations (10, 50, 100 and 200 μg/mL) of bismuthene for 24 h. Cell viability was analyzed by flow cytometry using Fixable Viability Dye 780 staining (BD). Ethanol at 70% was used as a positive control, while samples incubated with medium alone were used as negative controls. Histograms showing live and dead cells as % of positive cells. All the experiments were performed in triplicate and shown as means ± SD (Two-Way ANOVA and student T Test). **(b)** PBMCs were treated with bismuthene (100 μg/mL) for 24 h or left untreated (Unt), LPS (2 μg/mL) and ConA (10 μg/mL, Sigma) were used as positive controls. Cell activation was evaluated by flow cytometry, PBMCs were gated by specific membrane markers for the two major subpopulations: T cells (CD3-FITC, Clone: UCHT1, BD) and monocytes (CD16 BV711, Clone 3G8, BD). Cells were stained with CD25-PE and CD69-FITC. Cell activation of PBMCs was expressed as % of positive cells. Histogram plots showing positivity for CD25-PE (Clone M-A251, BD) and CD69-BV421 (Clone FN50, BD) staining in PBMCs treated with bismuthene (100 μg/mL) Data are presented as mean ± SD of three independent samples. *, $p < 0.05$; **, $p < 0.01$; ***, $p < 0.001$ (two-way ANOVA). **(c)** Cytokine production. IL-4, IL-5, IL-6, IL-10, IL-12, TNFα and IFNγ concentration measured in the supernatant of PBMCs treated with bismuthene (100 μg/mL) for 24 h, using BD Cytometric Bead Array(CBA) Kit.

4. Experimental section

4.1. Synthesis of 3D layered Bi amd the preparation of bismuthene nanosheets

3D layered bismuth was synthesized by using our established procedure [31]. All the sythesis was performed in a specially designed four-necked glass reactor system allowing it to work in an inert gas atmosphere (Argon) with an ability to temperature control. In a typical procedure, bismuth(III)chloride (BiCl$_3$, 98+%, Sigma-Aldrich) was used as a bismuth precursor, oleylamine (OAm, 70%, Sigma-Aldrich) was used as both surfactant and solvent, and also borane-tert-butylamine (BTB, 97%, Sigma-Aldrich) was used as a reducing agent. To get 3D layered bismuth, BiCl$_3$ in OAm solution was degassed in an inert argon atmosphere at 120 °C for 30 min, and then BTB-OAm complex was injected into the reactor system at the same temperature for additional 30 min (The color of the solution changed colorless to gray was observed). After that, the temperature was turned off and the system was allowed to cool itself to room temperature. The obtained solution was washed with ethanol three times to remove undesirable impurities via centrifuge at 8500 rpm for 10 min. The resultant black powder was dried at 40 °C in a vacuum oven and stored for later use.

For the preparation of bismuthene, as-prepared 3D layered bismuth was exfoliated in 2-propanol (pure, Iso Lab), under ambient conditions by ultrasonic homogenizer using a Bandelin Sonopuls 2200.2, 200 W, 40% amplitude, 1 h at 8–10 °C. A prepared bismuthene was separated from 2-propanol by centrifugation and dried overnight in a vacuum oven at 40 °C for solvent exchange. Bismuthene was exfoliated in DI water under ambient conditions via an ultrasonic bath, Bandelin SONOREX SUPER, 640 W, 6 h to prepare a bismuthene-DI water solution at 15–20 °C.

4.2. Characterization of bismuthene

The powder X-ray patterns (XRD) were recorded on a D2 Phaser Bruker with an X-ray source of CuKα radiation (λ = 1.5418 Å), 30 kV, 10 mA by step scanning with a step size of 0.02°, an interval of 1 s per step in the range of 2θ = 10–90°, to identify crystalline phases present. Thermo K-Alpha X-ray photoelectron spectrometer (XPS) equipped with Al−Kα (1468.3 eV) source was employed to analyze the surface chemistry of the prepared materials. Scanning electron microscopy (SEM) images were investigated with Zeiss Ultra Plus Field Emission Scanning Electron Microscope. Atomic force microscopy (AFM) measurements were taken using Bruker Dimension Icon AFM on the drop-cast flakes on a high-quality silicon wafer. Transmission electron microscopy (TEM), high angle annular dark field (HAADF) scanning transmission microscope (STEM) images, and the associated EDS elemental mappings were conducted on a Hitachi HT7800 (TEM) with EXALENS (120 kV) working at high-resolution (HR) mode. HRTEM images were taken on a Hitachi HF5000 with high-brightness, cold FEG-high stability, automated aberration corrector, and accelerating voltage at 200 kV. GATAN Digital-Micrograph® software was used to review HR-TEM image. UV–vis spectra were performed with Shimadzu 3600 Plus UV–Vis–NIR instrument. Raman spectra were carried out by using a Renishaw in Via Raman microscope (excitation source 633 nm) on Indium Tin Oxide (ITO) coated glass. A zeta-sizer and zeta potential (Malvern Instruments) were obtained for hydrodynamic diameter measurements. The results were performed in triplicates.

4.3. Magnetic analysis

AC susceptibility (χ) measurements were also performed at 40, 50, and 60 Hz frequencies under applied magnetic fields of 5, 10, and 15 Oe by using Physical Properties Measurement System (PPMS) with Vibrating Sample Module (VSM). The temperature dependence of magnetization (*M-T*) measurements were carried out under zero-field cooled (ZFC), and field cooled (FC) conditions from 5 to 350 K, and the magnetic field dependence magnetization (*M-H*) measurements were recorded at 5, 37, 50, 300, 320, and 350 K temperatures.

4.4. In vitro PTT and MH

A549 cell line, purchased from ATCC grown in DMEM high-glucose complete medium was trypsinized and inoculated into well plates or flasks according to the type of experiment. After overnight incubation, cells were incubated with bismuthene at different concentrations (0, 10, 50, 100, 200 μg/mL) for 4 h at 37 °C and 5% CO$_2$. After 4 h of bismuthene incubation, the medium was removed, and the cells were washed with DPBS, and fresh complete media were added. Depending on the type of experiment, cells were exposed to 50 W LED light of different wavelengths (520, 590, 625, 850, 940 nm) for different times (30 min, 1 h, 2 h) at room temperature. The power density was measured with a luminometer, and it was found to be 32.6 lm/cm^2 for all light sources as calculated before [8]. At the end of these periods, the cells were incubated at 37 °C and 5% CO$_2$, depending on the type of experiment. The groups with magnetic field application were exposed to 50 Hz 600 mA magnetic field for 1 h immediately after light exposure and then incubated.

4.5. Modified LDH assay

The A549 cell line was trypsinized and seeded into 96 well plates at 5×10^3 cells per well and then incubated at 37 °C and 5% CO$_2$ for 24 h. After incubation, cells were exposed to the *in vitro* PTT and application of magnetic field process. A cellular cytotoxicity assay was performed according to the LDH Cytotoxicity assay kit (Thermo) according to the modified protocol as discussed in Ali-Boucetta et al. [82]. 5 replicates were performed for each experimental group. LDH measurement absorbance was taken at 490 nm and 680 nm in the Clariostar Microplate Reader.

4.6. Flow cytometry analysis

A549 cell line was trypsinized and seeded into T25 flasks with 6×10^5 cells. It was removed by trypsinization for apoptosis analysis 12 h after exposure to *in vitro* PTT and application of magnetic field process. Apoptosis assay was performed according to the Alexa Flour 488 Annexin V assay kit (Thermo). To analyze the expression of calreticulin on cell surface cells were trypsinized following each treatment and washed with 1% BSA in PBS. Cells were first stained with an *anti*-calreticulin antibody (Thermo) and later with an anti-rabbit secondary antibody (Abcam). Three replicates were made for each experimental group. Flow Cytometry analysis was performed on the BD Accuri Plus instrument. 10,000 events were read for each sample. The obtained data were analyzed in BD Accuri Plus software.

4.7. ATP and HMGB1 assays

Following *in vitro* PTT and magnetic hyperthermia protocol, cell culture supernatants obtained from 1×10^6 cells) were collected. Samples were run on ATP assay (Promega) or HMGB1 assay (eLabio-sciences). Assays were performed according to the manufacturers' protocols.

4.8. MDA and GSH/GSSG assays

MDA assay was performed via the Lipid Peroxidation MDA Assay Kit (E-BC-K025-M, elabscience). The samples (obtained from 1×10^6 cells) and standards were prepared and the OD value was measured at 532 nm. The levels of GSH (reduced glutathione)/GSSG (oxidized glutathione disulfide) were measured using a GSH/GSSG ratio detection assay kit (E-BC-K097-M, elabscience).

4.9. qRT-PCR

Cells (1×10^6) were harvested for RNA extraction by using Machery Nagel RNA extraction kit following manufacturer's protocol. RNA samples were measured using Nanodrop ND-1000 Spectrophotometer (Thermo Fisher Scientific, Illinois, USA). Reverse transcription process was performed by using NG dART Kit (EURx, Poland) following manufacturer's protocol. PCR was performed by LightCycler®384 instrument (Roche, OR, USA) in the presence of Eva Green (EURx, Poland). Five ferroptosis-related primers were used in the study and genes were standardized to GAPDH housekeeping genes. $2^{\Delta\Delta Ct}$ method was used for analysis.

4.10. TEM

A549 cell line was seeded in T25 flasks at 60–70% confluent. Two groups were obtained after overnight incubation, a control group, and a bismuthene-treated group. Adherent cells (A549) were washed twice with PBS and then resuspended in PBS. Cells were removed from the bottom of the flasks by cell scraping, transferred to 1.5 mL polypropylene tubes, and centrifuged ($200 \times g$ for 10 min, 4 °C). The supernatant was discarded. Cells were gently fixed in 1 mL 2.5% glutaraldehyde in 0.1 M sodium cacodylate buffer, pH 7.2 at room temperature for 2 h followed by a further fixation at 4 °C overnight. Next, cells were washed in 0.1 M sodium cacodylate buffer and postfixed in 2% osmium tetroxide (OsO4). Post-fixation was followed by several washes and staining 1 h in 2% uranyl acetate. Afterward, cells were twice dehydrated on a rotor at room temperature for over 15 min using a graded ethanol series: 50%, 70%, 90%, and 100%. This was followed by specimen embedding in Araldite M mixtures and was performed according to standard procedures. Blocks were then trimmed, semithin sectioned. Subsequently, thin sections were cut and transferred onto copper mesh grids. First, the grids were stained in 2% uranyl acetate and then with lead citrate. The grids were studied with a CARL ZEISS EVO LS 10.

4.11. Fluorescent microscopy

To detect ROS, cells were seeded in a 24 well plate with 25,000 cells per well. After 24 h of incubation, cells were treated with bismuthene for 4 h. According to the Oxygen Species Detection Kit (abcam) protocol, medium was replaced with fresh medium, and stained. Then, according to the *in vitro* PTT application, they were treated with light for 1 h. Fixed cells were counterstained with 4′,6-diamidino-2-phenylindole (DAPI). Images were analyzed under the EVOS fluorescence microscope. The same kit was also used to detect ROS in tumor sections. For this analysis, sections were deparaffinized and stained with the DCFDA solution for 45 min. Following washing, sections were counterstained with DAPI and imaged.

4.12. In vivo PTT and application of magnetic field

Female BALB/c nude mice 8 weeks old (22–25g each), 5 groups (5 mice in each group) were obtained from Research Unit for Experimental Animals in Bilkent University, Turkey. All the experiments have been performed under the ethical approval of the local ethical committee of Bilkent University and the study design was planned according to the ARRIVE 2.0 guidelines. The A549 cell line (2×10^6 cells) PBS:Matrigel (Corning Ref:356,234) (1:1) was prepared for the xenograft model. All mice received a subcutaneous injection of 100 µL from the right of the lumbar region median line. A standard 26 G insulin injection was used. Tumor sizes and body weights of mice were monitored. Mice were anesthetized with isoflurane when their tumor size reached approximately 200 mm³. When the tumor size reached the desired size, the mice were randomly divided into groups. According to the experimental group, bismuthene (1000 µg in 100 µL dH2O) was injected through the

tail vein. To complete the PTT and magnetic field applications according to the determined experimental groups, they were exposed to 850 nm light (1 h with same power density calculated for *in vitro* experimentation) under isofluorescent anesthesia 1 h after the injection. These PTT and magnetic field applications were repeated 4 times. Naïve group corresponds the animals injected only with saline and there is no light irradiation or magnetic field exposure.

4.13. ICP-MS analysis

To observe biodistribution, xenograft models were divided into 2 groups (control and bismuthene-treatment), and the bismuthene-treatment group was injected with tail vein bismuthene (1000 µg in 100 µL dH2O). After 24 h, animals in both groups were sacrificed, and their organs were dissected. Dissected organs were washed with PBS and frozen at −80 °C. Tissues frozen for ICP-MS analysis were thawed and allowed to dry in an oven at 50–55 °C for 3 days. After making sure that the water in the tissues was completely evaporated, the tissues were powdered in a lab mortar with the help of liquid nitrogen. ICP-MS analysis was performed at Koç University. Inductively Coupled Plasma-Mass Spectrometer (ICP-MS) analysis were performed on an Agilent 7700x. For the ICP-MS analysis, the powder samples were digested in 10 mL aqua regia (8 mL HNO_3 + 2 mL HCl) via Start D Milestone Microwave Digestion system and obtained samples diluted at 1:3 ratio with deionized water (18.2 Mohm) blank solution.

4.14. Histological analysis

Once tumor specimen was resected, they were immediately fixed in 10% neutral buffered formalin (NBF). All specimens were processed uniformly and according to routine histological tissue processing steps [8]. The sections were stained with Masson's trichrome stain and mounted with Entellan. IHC staining of the tumor samples were performed concurrently on serial sections with the standard streptavidin-biotin complex method. After deparaffinization and rehydration steps, endogenous peroxidase activity was blocked by quenching with 3% hydrogen peroxide solution for 15 min. Next, a heat-induced epitope retrieval method was performed with sodium citrate (10 mM, pH 6) to remove the methylene bridges between proteins. Sequentially, sections were incubated with 10% normal rabbit serum for 30 min for protein blocking, followed by incubation with CD11c primary antibody (PA5-90208, Thermofisher, IL, US) and CD56 (NCAM) (PA5-78402, Thermofisher, IL, US) at dilution of 1:400 for 2 h. After a TBS wash, sections were incubated with biotinylated anti-rabbit antibody (IgG BA1000, Vector Laboratories Inc., CA, USA) for 30 min. Following another washing step, peroxidase-conjugated streptavidin reagent (Standard Vectastain Elite ABC Kit, PK-6100, Vector Laboratories Inc, CA, USA) was added for 30 min. Then sections were incubated in a peroxidase substrate solution DAB (3,3′-diaminobenzidine substrate, SK-4100, Vector Laboratories Inc, CA, USA). The sections were then counterstained with Gill's (III) hematoxylin and coverslipped. Slides were viewed under a digital camera (DFC450, Leica, Wetzlar, Germany) and integrated light microscope (DM2500, Leica, Wetzlar, Germany).

4.15. Peripheral blood mononuclear cells (PBMCs)

Peripheral Blood Mononuclear Cells (PBMCs) were collected from ethylenediamine tetraacetic acid (EDTA)-venous blood of healthy volunteers (25–50 years old) following the Ficoll-Paque (GE Healthcare, CA, USA) standard separation protocol. The signature of informed consent was obtained from all participants. The Ethics Committee of the University of Padua reviewed and approved all the protocols performed. Cell isolation and treatment were performed directly after blood draw. PBMCs were cultured in 24-well plates in RPMI 1640 medium (Life Technologies), supplemented with 1% penicillin/streptomycin (Life Technologies), and 10% heat-inactivated fetal bovine serum (Life

Technologies). Experiments were conducted using at least three healthy donors each in technical triplicate.

4.16. Hemolysis

100 μL of fresh human whole blood (1×10^6 cells) was harvested from informed, healthy donors (25–50 years old) using a Ficoll-Paque (GE Healthcare, CA, USA) standard separation protocol. Informed signed consent was obtained from all the donors. The Ethics Committee of the University of Padua reviewed and approved all the protocols performed. Blood was stabilized with ethylenediamine tetraacetic acid (EDTA). Serum was removed from blood samples by centrifugation at 200 g for 5 min. RBCs were washed three times and then diluted with sterile isotonic PBS. To determine the hemolytic activity, bismuthene (100 μg/mL) suspended in water, was added to RBCs suspension in a final volume of 1 mL PBS. After vortexing, the mixtures were left at 37 °C in a Thermo mixer at 500/600g for 1 and 24 h. At the end of the incubation times, RBCs were removed by centrifugation. A microplate reader (Sunrise TECAN Infinite M200PRO) measured the absorbance of the hemoglobin in the supernatant at 570 nm, with the absorbance at 620 nm as a reference.

4.17. Blood counts

250 μL of whole human blood was harvested from a healthy donor and incubated with 100 μg/mL bismuthene suspended in water or left untreated (Unt). After 24 h, complete blood counts were performed. Changes in the number of red blood cells (RBC), platelets (PLT), total white blood cells (WBC), then divided into neutrophils (NEUTR), lymphocytes (LYMPH), and monocytes (MONO), were analyzed. Changes in hematocrit (HCT), amount of hemoglobin (HGB), mean corpuscular volume (MCV), mean corpuscular hemoglobin (MCH) and its concentration (MCHC), red blood cell distribution width (RDW), and hemoglobin distribution width (HDW) were also monitored.

4.18. Cytotoxicity

1×10^6 PBMCs were treated with increasing concentrations (10, 50, 100, and 200 μg/mL) of bismuthene suspended in water for 24 h, and Fixable Viability Stain 780 (FVS780, BD Horizon™) was used to assess cell viability. Staining was performed in the dark for 30 min. Ethanol at 70% was used as a positive control, while samples incubated only with medium were used as negative controls. Cells were processed by flow cytometry (LSR Fortessa X-20, BD Bioscience, CA, USA), while data were analyzed by FlowJo™

4.19. Analysis of PBMCs activation by flow cytometry

1×10^6 PBMCs were treated with 100 μg/mL of bismuthene suspended in water for 24 h. Cell activation was evaluated by flow cytometry, PBMCs were gated by specific membrane markers for the two major subpopulations: T cells (CD3-FITC, Clone: UCHT1, BD) and monocytes (CD16 BV711, Clone 3G8, BD). Cells were stained with CD25 (PE-conjugated anti-CD25, M-A251 clone; BD Bioscience, CA, USA) and CD69 (BV421-conjugated anti-CD69, FN50 clone; BD Bioscience, CA, USA). Staining was performed in the dark for 30 min. LPS (2 μg/mL, Sigma) and ConA (2 μg/mL, Sigma) were used as positive controls. Cells were processed by flow cytometry (LRS Fortessa, BD Bioscience, CA, USA), and data were analyzed by FlowJo™ Software.

4.20. Multiplex cytokine analysis

Cell culture supernatants from PBMCs after treatment with bismuthene (100 μg/mL) suspended in water, were used to quantify the secretion of cytokines using a Cytometric Bead Array (CBA) immunoassay kit (BD Biosciences, USA). Concanavalin A (ConA, 10 μg/mL) and lipopolysaccharides (LPS 2 μg/mL) were used as positive controls. The following human cytokines were measured: IL-4, IL-5, IL-6, IL-10, TNF-α, IFN-γ and IL-12p70. Samples were treated according to the manufacturer's protocol. Data were acquired in a BD LRS Fortessa flow cytometry system (BD Biosciences, San Jose, CA, USA), and analyses were performed using BD FCAP Array v3.0 software (BD Biosciences, San Jose, CA, USA). The standard curve was determined using a five-parameter logistic (5-PL) equation. The results were based on a standard concentration curve and expressed as picogram per milliliter (pg/mL).

4.21. Statistical analysis

The values obtained with GraphPad statistical programme are expressed as mean ± ST.D. Comparison between groups was performed by one-way ANOVA followed by Tukey's post hoc multiple comparisons. Analyses were performed according to 3 independent technical replicates. For *in vitro* experiments, 8 biological replicates were used. For *in vivo* experiments, 5 mice were used under each group.

Author contributions

Açelya Yilmazer *1,2, Conceptualization, Funding acquisition, Project administration, Supervision Roles/Writing - original draft; and Writing - review & editing. Zafer Eroglu3, Data curation; Methodology; Validation; Visualization; Roles/Writing - original draft; and Writing - review & editing, Cansu Gurcan1,2, Data curation; Methodology; Validation; Visualization; Roles/Writing - original draft; and Writing - review & editing, Arianna Gazzi4,5, Data curation; Methodology; Validation; Visualization; Roles/Writing - original draft Okan Ekim6, Methodology; Supervision; Validation, Buse Sundu3, Data curation; Methodology; Validation, Cemile Gokce1, Data curation; Methodology; Roles/Writing - original draft; and Writing - review & editing, Ahmet Ceylan7, Data curation; Methodology; Visualization; Roles/Writing - original draft, Linda Giro4, Data curation; Methodology; Roles/Writing - original draft; and Writing - review & editing, Mehmet Altay Unal2, Methodology; Software; Supervision, Fikret Arı8, Methodology; Software, Ahmet Ekicibil9, Data curation; Methodology; Roles/Writing - original draft; Ozge Ozgenç Çinar7, Data curation; Methodology; Visualization, Berfin Ilayda Ozturk1, Data curation; Methodology, Omur Besbinar1,2, Data curation; Methodology, Mine Ensoy10, Methodology; Roles/Writing - original draft, Demet Cansaran-Duman10, Methodology; Roles/Writing - original draft, Lucia Gemma Delogu4*, Conceptualization, Funding acquisition, Project administration, Supervision Roles/Writing - original draft; and Writing - review & editing. Onder Metin*3, 11 Conceptualization, Funding acquisition, Project administration, Supervision Roles/Writing - original draft; and Writing - review & editing.

Declaration of competing interest

The authors declare that there is no conflict of interest.

Data availability

Data will be made available on request.

study illustration in Fig. 1.

Appendix A. Supplementary data

Supplementary data to this article can be found online at https://doi.org/10.1016/j.mtbio.2023.100825.

References

[1] H. Sung, J. Ferlay, R.L. Siegel, M. Laversanne, I. Soerjomataram, A. Jemal, F. Bray, Global cancer Statistics 2020: GLOBOCAN estimates of incidence and mortality worldwide for 36 cancers in 185 countries, CA A Cancer J. Clin. 71 (3) (2021) 209–249, https://doi.org/10.3322/caac.21660.

[2] Y. Hao, C.K. Chung, Z. Yu, R.V. Huis, t Veld, F.A. Ossendorp, P. Ten Dijke, L. J. Cruz, Combinatorial therapeutic approaches with nanomaterial-based photodynamic cancer therapy, Pharmaceutics 14 (1) (2022), https://doi.org/10.3390/pharmaceutics14010120.

[3] B.L. Melo, R. Lima-Sousa, C.G. Alves, A.F. Moreira, I.J. Correia, D. de Melo-Diogo, Chitosan-based injectable in situ forming hydrogels containing dopamine-reduced graphene oxide and resveratrol for breast cancer chemo-photothermal therapy, Biochem. Eng. J. 185 (2022), 108529, https://doi.org/10.1016/j.bej.2022.108529.

[4] M. Doroudian, S. Zanganeh, E. Abbasgholinejad, S.C. Donnelly, Nanomedicine in lung cancer immunotherapy, Front. Bioeng. Biotechnol. 11 (2023), 1144653, https://doi.org/10.3389/fbioe.2023.1144653.

[5] H. Chen, T. Liu, Z. Su, L. Shang, G. Wei, 2D transition metal dichalcogenide nanosheets for photo/thermo-based tumor imaging and therapy, Nanoscale Horiz 3 (2) (2018) 74–89, https://doi.org/10.1039/C7NH00158D.

[6] P. Zhang, C. Hu, W. Ran, J. Meng, Q. Yin, Y. Li, Recent progress in light-triggered nanotheranostics for cancer treatment, Theranostics 6 (7) (2016) 948–968, https://doi.org/10.7150/thno.15217.

[7] A. Gazzi, L. Fusco, A. Khan, D. Bedognetti, B. Zavan, F. Vitale, A. Yilmazer, L. G. Delogu, Photodynamic therapy based on graphene and MXene in cancer theranostics, Front. Bioeng. Biotechnol. 7 (2019), https://doi.org/10.3389/fbioe.2019.00295, 295-295.

[8] H. Taheri, M.A. Unal, M. Sevim, C. Gurcan, O. Ekim, A. Ceylan, Z. Syrgiannis, K. C. Christoforidis, S. Bosi, O. Ozgenç, M.J. Gómez, M. Turktas Erken, Ç. Soydal, Z. Eroğlu, C.V. Bitirim, U. Cagin, F. Arı, A. Ozen, O. Kuçuk, L.G. Delogu, M. Prato, Ö. Metin, A. Yilmazer, Photocatalytically active graphitic carbon nitride as an effective and safe 2D material for in vitro and in vivo photodynamic therapy, Small 16 (10) (2020), 1904619, https://doi.org/10.1002/smll.201904619.

[9] Y.J. Hou, X.X. Yang, R.Q. Liu, D. Zhao, C.X. Guo, A.C. Zhu, M.N. Wen, Z. Liu, G. F. Qu, H.X. Meng, Pathological mechanism of photodynamic therapy and photothermal therapy based on nanoparticles, Int. J. Nanomed. 15 (2020) 6827–6838, https://doi.org/10.2147/ijn.S269321.

[10] W. Li, J. Yang, L. Luo, M. Jiang, B. Qin, H. Yin, C. Zhu, X. Yuan, J. Zhang, Z. Luo, Y. Du, Q. Li, Y. Lou, Y. Qiu, J. You, Targeting photodynamic and photothermal therapy to the endoplasmic reticulum enhances immunogenic cancer cell death, Nat. Commun. 10 (1) (2019) 3349, https://doi.org/10.1038/s41467-019-11269-8.

[11] P. An, Z. Gao, K. Sun, D. Gu, H. Wu, C. You, Y. Li, K. Cheng, Y. Zhang, Z. Wang, B. Sun, Photothermal-enhanced inactivation of glutathione peroxidase for ferroptosis sensitized by an autophagy promotor, ACS Appl. Mater. Interfaces 11 (46) (2019) 42988–42997, https://doi.org/10.1021/acsami.9b16124.

[12] F. Zeng, L. Tang, Q. Zhang, C. Shi, Z. Huang, S. Nijiati, X. Chen, Z. Zhou, Coordinating the mechanisms of action of ferroptosis and the photothermal effect for cancer theranostics, Angew Chem. Int. Ed. Engl. 61 (13) (2022), e202112925, https://doi.org/10.1002/anie.202112925.

[13] C. Wu, Z. Liu, Z. Chen, D. Xu, L. Chen, H. Lin, J. Shi, A nonferrous ferroptosis-like strategy for antioxidant inhibition-synergized nanocatalytic tumor therapeutics, Sci. Adv. 7 (39) (2021), eabj8833, https://doi.org/10.1126/sciadv.abj8833.

[14] H. Huang, C. Dong, W. Feng, Y. Wang, B. Huang, Y. Chen, Biomedical engineering of two-dimensional MXenes, Adv. Drug Deliv. Rev. 184 (2022), 114178, https://doi.org/10.1016/j.addr.2022.114178.

[15] H. Huang, W. Feng, Y. Chen, Two-dimensional biomaterials: material science, biological effect and biomedical engineering applications, Chem. Soc. Rev. 50 (20) (2021) 11381–11485, https://doi.org/10.1039/D0CS01138J.

[16] B. Luo, G. Liu, L. Wang, Recent advances in 2D materials for photocatalysis, Nanoscale 8 (13) (2016) 6904–6920, https://doi.org/10.1039/C6NR00546B.

[17] S. Yadav, M.A. Sadique, A. Kaushik, P. Ranjan, R. Khan, A.K. Srivastava, Borophene as an emerging 2D flatland for biomedical applications: current challenges and future prospects, J. Mater. Chem. B 10 (8) (2022) 1146–1175, https://doi.org/10.1039/d1tb02277f.

[18] W. Zeng, H. Zhang, X. Yuan, T. Chen, Z. Pei, X. Ji, Two-Dimensional Nanomaterial-based catalytic Medicine: theories, advanced catalyst and system design, Adv. Drug Deliv. Rev. 184 (2022), 114241, https://doi.org/10.1016/j.addr.2022.114241.

[19] W. Zhu, H. Li, P. Luo, Emerging 2D nanomaterials for multimodel theranostics of cancer, Front. Bioeng. Biotechnol. 9 (2021), 769178, https://doi.org/10.3389/fbioe.2021.769178.

[20] L. Chen, Z. Wang, F. Liu, Robustness of two-dimensional topological insulator states in bilayer bismuth against strain and electrical field, Phys. Rev. B 87 (23) (2013), 235420.

[21] L. Cheng, H. Liu, X. Tan, J. Zhang, J. Wei, H. Lv, J. Shi, X. Tang, Thermoelectric properties of a monolayer bismuth, J. Phys. Chem. C 118 (2) (2014) 904–910.

[22] X. Wang, G. Bian, C. Xu, P. Wang, H. Hu, W. Zhou, S. Brown, T. Chiang, Topological phases in double layers of bismuthene and antimonene, Nanotechnology 28 (39) (2017), 395706.

[23] P. Guo, X. Li, T. Feng, Y. Zhang, W. Xu, Few-layer bismuthene for coexistence of harmonic and dual wavelength in a mode-locked fiber laser, ACS Appl. Mater. Interfaces 12 (28) (2020) 31757–31763, https://doi.org/10.1021/acsami.0c05325.

[24] G.G. Briand, N. Burford, Bismuth compounds and preparations with biological or medicinal relevance, Chem. Rev. 99 (9) (1999) 2601–2658, https://doi.org/10.1021/cr980425s.

[25] E. Aktürk, O.Ü. Aktürk, S. Ciraci, Single and bilayer bismuthene: stability at high temperature and mechanical and electronic properties, Phys. Rev. B 94 (1) (2016), 014115, https://doi.org/10.1103/PhysRevB.94.014115.

[26] W. Huang, J. Zhu, M. Wang, L. Hu, Y. Tang, Y. Shu, Z. Xie, H. Zhang, Emerging mono-elemental bismuth nanostructures: controlled synthesis and their versatile applications, Adv. Funct. Mater. 31 (10) (2021), 2007584, https://doi.org/10.1002/adfm.202007584.

[27] B. Ma, R.-T. Liu, X.-D. Zhang, Q. Wang, H.-L. Zhang, Ultrafast generation of coherent phonons in two-dimensional bismuthene, J. Phys. Chem. Lett. 13 (13) (2022) 3072–3078.

[28] A. Saffarzadeh, G. Kirczenow, Resonant and nonresonant spin filtering in bismuthene-silicon cowrie shell-like nanostructures, Phys. Rev. B 104 (15) (2021), 155406.

[29] S.M. Beladi-Mousavi, Y. Ying, J. Plutnar, M. Pumera, Bismuthene metallurgy: transformation of bismuth particles to ultrahigh-aspect-ratio 2D microsheets, Small 16 (29) (2020), 2002037.

[30] E.S. Walker, S.R. Na, D. Jung, S.D. March, J.S. Kim, T. Trivedi, W. Li, L. Tao, M. L. Lee, K.M. Liechti, D. Akinwande, S.R. Bank, Large-area dry transfer of single-crystalline epitaxial bismuth thin films, Nano Lett. 16 (11) (2016) 6931–6938, https://doi.org/10.1021/acs.nanolett.6b02931.

[31] M.S. Ozer, Z. Eroglu, A.S. Yalin, M. Kılıç, U. Rothlisberger, O. Metin, Bismuthene as a versatile photocatalyst operating under variable conditions for the photoredox CH bond functionalization, Appl. Catal., B 304 (2022), 120957, https://doi.org/10.1016/j.apcatb.2021.120957.

[32] R. Chai, L. Yu, C. Dong, Y. Yin, S. Wang, Y. Chen, Q. Zhang, Oxygen-evolving photosynthetic cyanobacteria for 2D bismuthene radiosensitizer-enhanced cancer radiotherapy, Bioact. Mater. 17 (2022) 276–288.

[33] V. Urbanová, M. Pumera, Biomedical and bioimaging applications of 2D pnictogens and transition metal dichalcogenides, Nanoscale 11 (34) (2019) 15770–15782.

[34] Y. Wang, W. Feng, M. Chang, J. Yang, Y. Guo, L. Ding, L. Yu, H. Huang, Y. Chen, J. Shi, Engineering 2D multifunctional ultrathin bismuthene for multiple photonic nanomedicine, Adv. Funct. Mater. 31 (6) (2021), 2005093.

[35] L. Bai, W. Yi, J. Chen, B. Wang, Y. Tian, P. Zhang, X. Cheng, J. Si, X. Hou, J. Hou, Two-stage targeted bismuthene-based composite nanosystem for multimodal imaging guided enhanced hyperthermia and inhibition of tumor recurrence, ACS Appl. Mater. Interfaces 14 (22) (2022) 25050–25064, https://doi.org/10.1021/acsami.2c01128.

[36] Y. Zhu, Y. Wu, S. Li, X. Yuan, J. Shen, S. Luo, Z. Wang, R. Gao, J. Wu, L. Ge, Photocatalytic and photothermal bismuthene nanosheets as drug carrier capable of generating CO to improve drug sensitivity and reduce inflammation for enhanced cancer therapy, Chem. Eng. J. 446 (2022), 137321, https://doi.org/10.1016/j.cej.2022.137321.

[37] M. Guo, X. Zhang, J. Liu, F. Gao, X. Zhang, X. Hu, B. Li, X. Zhang, H. Zhou, R. Bai, Few-layer bismuthene for checkpoint knockdown enhanced cancer immunotherapy with rapid clearance and sequentially triggered one-for-all strategy, ACS Nano 14 (11) (2020) 15700–15713.

[38] N. Hossain, M.A. Chowdhury, S. Sultana, R. Nandee, Scope of 2D materials for immune response-a review, Results Eng 14 (2022), 100413.

[39] L. Fusco, A. Gazzi, C.E. Shuck, M. Orecchioni, E.I. Ahmed, L. Giro, B. Zavan, A. Yilmazer, K. Ley, D. Bedognetti, V4C3 MXene immune profiling and modulation of T cell-dendritic cell function and interaction, Small Methods (2023), 2300197.

[40] L. Fusco, A. Gazzi, C.E. Shuck, M. Orecchioni, D. Alberti, S.M. D'Almeida, D. Rinchai, E. Ahmed, O. Elhanani, M. Rauner, Immune profiling and multiplexed label-free detection of 2D MXenes by mass cytometry and high-dimensional imaging, Adv. Mater. 34 (45) (2022), 2205154.

[41] A.F. Rodrigues, L. Newman, D.A. Jasim, I.A. Vacchi, C. Ménard-Moyon, L.E. Crica, A. Bianco, K. Kostarelos, C. Bussy, Immunological impact of graphene oxide sheets in the abdominal cavity is governed by surface reactivity, Arch. Toxicol. 92 (11) (2018) 3359–3379, https://doi.org/10.1007/s00204-018-2303-z.

[42] L. Lu, Z. Liang, L. Wu, Y. Chen, Y. Song, S.C. Dhanabalan, J.S. Ponraj, B. Dong, Y. Xiang, F. Xing, D. Fan, H. Zhang, Few-layer bismuthene: sonochemical exfoliation, nonlinear optics and applications for ultrafast photonics with enhanced stability, Laser Photon. Rev. 12 (1) (2018), 1700221, https://doi.org/10.1002/lpor.201700221.

[43] F. Yang, A.O. Elnabawy, R. Schimmenti, P. Song, J. Wang, Z. Peng, S. Yao, R. Deng, S. Song, Y. Lin, M. Mavrikakis, W. Xu, Bismuthene for highly efficient carbon dioxide electroreduction reaction, Nat. Commun. 11 (1) (2020) 1088, https://doi.org/10.1038/s41467-020-14914-9.

[44] J. Zhang, S. Ye, Y. Sun, F. Zhou, J. Song, J. Qu, Soft-template assisted synthesis of hexagonal antimonene and bismuthene in colloidal solutions, Nanoscale 12 (40) (2020) 20945–20951, https://doi.org/10.1039/D0NR05578F.

[45] W. Zhang, Y. Hu, L. Ma, G. Zhu, P. Zhao, X. Xue, R. Chen, S. Yang, J. Ma, J. Liu, Liquid-phase exfoliated ultrathin Bi nanosheets: uncovering the origins of enhanced electrocatalytic CO2 reduction on two-dimensional metal nanostructure, Nano Energy 53 (2018) 808–816.

[46] J. Zhou, J. Chen, M. Chen, J. Wang, X. Liu, B. Wei, Z. Wang, J. Li, L. Gu, Q. Zhang, Few-layer bismuthene with anisotropic expansion for high-areal-capacity sodium-ion batteries, Adv. Mater. 31 (12) (2019), 1807874.

[47] Q.-Q. Yang, R.-T. Liu, C. Huang, Y.-F. Huang, L.-F. Gao, B. Sun, Z.-P. Huang, L. Zhang, C.-X. Hu, Z.-Q. Zhang, 2D bismuthene fabricated via acid-intercalated exfoliation showing strong nonlinear near-infrared responses for mode-locking lasers, Nanoscale 10 (45) (2018) 21106–21115.

[48] R.R. Kahmei, P. Seal, J. Borah, Tunable heat generation in nickel-substituted zinc ferrite nanoparticles for magnetic hyperthermia, Nanoscale Adv. 3 (18) (2021) 5339–5347.

[49] Y. Nosaka, A.Y. Nosaka, Generation and detection of reactive oxygen species in photocatalysis, Chem. Rev. 117 (17) (2017) 11302–11336, https://doi.org/10.1021/acs.chemrev.7b00161.

[50] X. Chen, C. Yu, R. Kang, G. Kroemer, D. Tang, Cellular degradation systems in ferroptosis, Cell Death Differ. 28 (4) (2021) 1135–1148.

[51] R. Kurapati, K. Kostarelos, M. Prato, A. Bianco, Biomedical uses for 2D materials beyond graphene: current advances and challenges ahead, Adv. Mater. 28 (29) (2016) 6052–6074.

[52] V. Shukla, The tunable electric and magnetic properties of 2D MXenes and their potential applications, Mater Adv 1 (9) (2020) 3104–3121.

[53] D.K. Nguyen, T.V. Bao, N.A. Kha, R. Ponce-Pérez, J. Guerrero-Sanchez, D. Hoat, Searching for d 0 spintronic materials: bismuthene monolayer doped with IVA-group atoms, RSC Adv. 13 (9) (2023) 5885–5892.

[54] J. Yu, F. Chen, W. Gao, Y. Ju, X. Chu, S. Che, F. Sheng, Y. Hou, Iron carbide nanoparticles: an innovative nanoplatform for biomedical applications, Nanoscale Horiz 2 (2) (2017) 81–88.

[55] X. Wu, H. Zhang, Therapeutic strategies of iron-based nanomaterials for cancer therapy, Biomed. Mater. 16 (3) (2021) 032003.

[56] W. Bao, X. Liu, Y. Lv, G.-H. Lu, F. Li, F. Zhang, B. Liu, D. Li, W. Wei, Y. Li, Nanolongan with multiple on-demand conversions for ferroptosis–apoptosis combined anticancer therapy, ACS Nano 13 (1) (2019) 260–273.

[57] S. Zanganeh, G. Hutter, R. Spitler, O. Lenkov, M. Mahmoudi, A. Shaw, J. S. Pajarinen, H. Nejadnik, S. Goodman, M. Moseley, Iron oxide nanoparticles inhibit tumour growth by inducing pro-inflammatory macrophage polarization in tumour tissues, Nat. Nanotechnol. 11 (11) (2016) 986–994.

[58] H. Yan, W. Shang, X. Sun, L. Zhao, J. Wang, Z. Xiong, J. Yuan, R. Zhang, Q. Huang, K. Wang, "All-in-one" nanoparticles for trimodality imaging-guided intracellular photo-magnetic hyperthermia therapy under intravenous administration, Adv. Funct. Mater. 28 (9) (2018) 1705710.

[59] G. Huang, J. Hu, H. Zhang, Z. Zhou, X. Chi, J. Gao, Highly magnetic iron carbide nanoparticles as effective T 2 contrast agents, Nanoscale 6 (2) (2014) 726–730.

[60] M. Xing, J. Mohapatra, J. Beatty, J. Elkins, N.K. Pandey, A. Chalise, W. Chen, M. Jin, J.P. Liu, Iron-based magnetic nanoparticles for multimodal hyperthermia heating, J. Alloys Compd. 871 (2021) 159475.

[61] L. Cheng, S. Shen, S. Shi, Y. Yi, X. Wang, G. Song, K. Yang, G. Liu, T.E. Barnhart, W. Cai, FeSe2-decorated Bi2Se3 nanosheets fabricated via cation exchange for chelator-free 64Cu-labeling and multimodal image-guided photothermal-radiation therapy, Adv. Funct. Mater. 26 (13) (2016) 2185–2197.

[62] R. Das, N. Rinaldi-Montes, J. Alonso, Z. Amghouz, E. Garaio, J.A. Garcia, P. Gorria, J.A. Blanco, M.-H. Phan, H. Srikanth, Boosted hyperthermia therapy by combined AC magnetic and photothermal exposures in Ag/Fe3O4 nanoflowers, ACS Appl. Mater. Interfaces 8 (38) (2016) 25162–25169.

[63] S. Nemec, S. Kralj, C. Wilhelm, A. Abou-Hassan, M.-P. Rols, J. Kolosnjaj-Tabi, Comparison of iron oxide nanoparticles in photothermia and magnetic hyperthermia: effects of clustering and silica encapsulation on nanoparticles' heating yield, Appl. Sci. 10 (20) (2020) 7322.

[64] S. Shaw, J. Kailashiya, A. Gangwar, S. Alla, S.K. Gupta, C. Prajapat, S.S. Meena, D. Dash, P.h. Maiti, N. Prasad, γ-Fe2O3 nanoflowers as efficient magnetic hyperthermia and photothermal agent, Appl. Surf. Sci. 560 (2021), 150025.

[65] A. Mantovani, P. Allavena, A. Sica, F. Balkwill, Cancer-related inflammation, Nature 454 (7203) (2008) 436–444.

[66] D.B. Vendramini-Costa, J. E carvalho, Molecular link mechanisms between inflammation and cancer, Curr. Pharmaceut. Des. 18 (26) (2012) 3831–3852.

[67] R. Molinaro, C. Corbo, M. Livingston, M. Evangelopoulos, A. Parodi, C. Boada, M. Agostini, E. Tasciotti, Inflammation and cancer: in medio stat nano, Curr. Med. Chem. 25 (34) (2018) 4208–4223.

[68] S. Dutz, R. Hergt, Magnetic nanoparticle heating and heat transfer on a microscale: basic principles, realities and physical limitations of hyperthermia for tumour therapy, Int. J. Hyperther. 29 (8) (2013) 790–800.

[69] M. Vasilakaki, C. Binns, K. Trohidou, Susceptibility losses in heating of magnetic core/shell nanoparticles for hyperthermia: a Monte Carlo study of shape and size effects, Nanoscale 7 (17) (2015) 7753–7762.

[70] T. Yamaminami, S. Ota, S.B. Trisnanto, M. Ishikawa, T. Yamada, T. Yoshida, K. Enpuku, Y. Takemura, Power dissipation in magnetic nanoparticles evaluated using the AC susceptibility of their linear and nonlinear responses, J. Magn. Magn Mater. 517 (2021), 167401.

[71] E. Hannachi, Y. Slimani, A.T. Okasha, G. Yasin, M. Iqbal, M. Shariq, D. Kaya, F. B. Azzouz, A. Ekicibil, YBCO superconductor added with one-dimensional TiO2 nanostructures: frequency dependencies of AC susceptibility, FC-ZFC magnetization, and pseudo-gap studies, J. Alloys Compd. 883 (2021), 160887.

[72] S. Sengupta, V.K. Balla, A review on the use of magnetic fields and ultrasound for non-invasive cancer treatment, J. Adv. Res. 14 (2018) 97–111.

[73] P. Wust, U. Gneveckow, M. Johannsen, D. Böhmer, T. Henkel, F. Kahmann, J. Sehouli, R. Felix, J. Ricke, A. Jordan, Magnetic nanoparticles for interstitial thermotherapy–feasibility, tolerance and achieved temperatures, Int. J. Hyperther. 22 (8) (2006) 673–685, https://doi.org/10.1080/02656730601106037.

[74] D. Kaya, I. Adanur, M. Akyol, F. Karadag, A. Ekicibil, Detailed investigation of structural and magnetic properties of multiphase binary Pd-Co alloys prepared by modified polyol process, J. Alloys Compd. 876 (2021) 160157, https://doi.org/10.1016/j.jallcom.2021.160157.

[75] S. Buchenau, S. Scheitz, A. Sethi, J.E. Slimak, T.E. Glier, P.K. Das, T. Dankwort, L. Akinsinde, L. Kienle, A. Rusydi, Temperature and magnetic field dependent Raman study of electron-phonon interactions in thin films of Bi 2 Se 3 and Bi 2 Te 3 nanoflakes, Phys. Rev. B 101 (24) (2020), 245431.

[76] D. Li, Y. Li, The interaction between ferroptosis and lipid metabolism in cancer, Signal Transduct. Targeted Ther. 5 (1) (2020) 108, https://doi.org/10.1038/s41392-020-00216-5.

[77] F. Zeng, L. Tang, Q. Zhang, C. Shi, Z. Huang, S. Nijiati, X. Chen, Z. Zhou, Coordinating the mechanisms of action of ferroptosis and the photothermal effect for cancer theranostics, Angew. Chem. Int. Ed. 61 (13) (2022), e202112925, https://doi.org/10.1002/anie.202112925.

[78] Y. Jiang, X. Zhao, J. Huang, J. Li, P.K. Upputuri, H. Sun, X. Han, M. Pramanik, Y. Miao, H. Duan, K. Pu, R. Zhang, Transformable hybrid semiconducting polymer nanozyme for second near-infrared photothermal ferrotherapy, Nat. Commun. 11 (1) (2020) 1857, https://doi.org/10.1038/s41467-020-15730-x.

[79] T. Yang, J. Zhai, D. Hu, R. Yang, G. Wang, Y. Li, G. Liang, "Targeting design" of nanoparticles in tumor therapy, Pharmaceutics 14 (9) (2022), https://doi.org/10.3390/pharmaceutics14091919.

[80] J. Shi, P.W. Kantoff, R. Wooster, O.C. Farokhzad, Cancer nanomedicine: progress, challenges and opportunities, Nat. Rev. Cancer 17 (1) (2017) 20–37, https://doi.org/10.1038/nrc.2016.108.

[81] S. Wilhelm, A.J. Tavares, Q. Dai, S. Ohta, J. Audet, H.F. Dvorak, W.C.W. Chan, Analysis of nanoparticle delivery to tumours, Nat. Rev. Mater. 1 (5) (2016), 16014, https://doi.org/10.1038/natrevmats.2016.14.

[82] H. Ali-Boucetta, K.T. Al-Jamal, K.H. Müller, S. Li, A.E. Porter, A. Eddaoudi, M. Prato, A. Bianco, K. Kostarelos, Cellular uptake and cytotoxic impact of chemically functionalized and polymer-coated carbon nanotubes, Small 7 (22) (2011) 3230–3238, https://doi.org/10.1002/smll.201101004.